Emergence of A-site cation order in the small rare-earth melilites Sr*RE*Ga$_3$O$_7$ (*RE* = Dy-Lu, Y)

Cécile Genevois[a], Haytem Bazzaoui[a], Marina Boyer[a], Sandra Ory[a], Yannick Ledemi[b], Younès Messaddeq[b], Michael J. Pitcher[a*] and Mathieu Allix[a*]

[a] CNRS, CEMHTI UPR 3079, Univ. Orléans, F-45071 Orléans, France. E-mail: mathieu.allix@cnrs-orleans.fr michael.pitcher@cnrs-orleans.fr

[b] Center for Optics, Photonics and Laser, Université Laval, Quebec City, Canada

KEYWORDS: Gallate melilite, metastability, cation ordering, luminescence, STEM-HAADF

ABSTRACT: Sr*RE*Ga$_3$O$_7$ melilite ceramics with large rare-earth elements (*RE* = La to Y) are famous materials especially known for their luminescence properties. Using an innovative approach, the full and congruent crystallization from glass process, Sr*RE*Ga$_3$O$_7$ transparent polycrystalline ceramics with small rare earth elements (*RE* = Dy-Lu and Y) have been successfully synthesized and characterized. Interestingly, compared to the classic tetragonal (P-42$_1m$) melilite structure composed of mixed Sr/*RE* cationic sites, these compositions can crystallize in a 3 x 1 x 1 orthorhombic ($P2_12_12$) superstructure. A detailed study of the superstructure, investigated by different techniques (synchrotron and neutron powder diffraction, STEM-HAADF imaging and EDS mapping), highlights the existence of a Sr/*RE* cation ordering favored by a large Sr/*RE* size mismatch and a sufficiently small *RE* cation. An appropriate control of the synthesis conditions through glass crystallization enables the formation of the desired polymorphs, either ordered or disordered. The influence of this tailored cationic ordering/disordering on the *RE* luminescent spectroscopic properties have been investigated. A stronger structuration of the *RE* emission band is observed in the ordered ceramic compared to the disordered ceramic and the glass, whose band shapes are very similar, indicating that the *RE* environment in the glass and disordered ceramic are close.

1. INTRODUCTION

The melilite gallates Sr*RE*Ga$_3$O$_7$ with the largest *RE* cations, i.e. *RE* = La to Y, are well known for their luminescence properties observed on single crystal or powder materials.[1–5] These compounds are readily synthesized by conventional ceramic methods and adopt the tetragonal melilite structure with a uniform [Ga$_3$O$_7$] framework layer and fully-disordered Sr/*RE* ("A-site") cations. In contrast, the compositions with *RE* smaller than Tm have not been widely studied, because they are challenging to synthesize, and they appear to have more complex structures that have not been fully characterized.[6,7] The introduction of small A-site cations (or more precisely, the imposition of a low A/B ionic radius ratio[8]) is known to induce distortions of the melilite framework, for example in the åckermanites Ca$_2$*M*Si$_2$O$_7$ (*M* = Mg^{2+}, Co^{2+})[9–11] and the gallates Ca*RE*Ga$_3$O$_7$ (*RE* = La, Nd)[8,12], which both have high concentrations of Ca^{2+} on the A-sites. These melilites undergo complex incommensurate structural distortions due to the size mismatch between the Ca/*RE*-sublattice and the tetrahedral framework layer, producing a modulated distribution of A-site environments ranging from 6- to 8-coordinate in CaNdGa$_3$O$_7$, which are better adapted for the local coordination of Ca^{2+} than the single 8-coordinate A-site exhibited in the undistorted parent phase.

An initial study of Sr*RE*Ga$_3$O$_7$ in the small-*RE* range (*RE* = Eu – Yb, Y) was motivated by the search for new luminescent transparent ceramics.[7] Transparent ceramics showing luminescence properties are key materials in the development of numerous applications such as laser gain media and scintillating inorganic materials.[13–18] Indeed, they combine the advantages of transparent media, such as volume excitation/emission, with ceramic optical emission properties, i.e. narrow and intense emission bands. Transparent ceramics are usually synthesized through complex powder sintering processes, requiring high temperature and high pressure to remove residual porosities acting like light scattering centers and consequently limiting the transparency of the resulting material.[16,19,20] An alternative synthesis approach, full crystallization from glass, was recently proposed to achieve transparent ceramics.[21–27] This process can lead to fully dense ceramics, i.e. ceramics without porosity, if the density difference between the

glass and the crystalline phases remains limited, thus preventing the appearance of cracks during crystallization. The full and congruent crystallization process also leads to very thin grain boundaries.[22] Therefore, the possibility to achieve fully dense ceramics with thin grain boundaries, two of the main requirements for transparent ceramics synthesis, has enabled the use of full glass crystallization to access new transparent ceramic compositions. This was particularly demonstrated for innovative materials showing non-cubic symmetry, as long as the birefringence effect remains limited.[7,21,22,28,29]

Moreover, crystallization from glass is a process operating at relatively low temperature compared to conventional powder sintering and solid state processes, thus offering the possibility to access new metastable crystalline phases as demonstrated for $BaAl_4O_7$,[21,30] $Sr_{1+x/2}Al_{2+x}Si_{2-x}O_8$,[22] $Sr_{1-x/2}Al_{2-x}Si_xO_4$,[28,31] and $Bi_{0.8}Nb_{0.8}Te_{2.4}O_8$ transparent ceramics.[32] Using this method, we were successful in synthesizing new transparent to Sr*RE*Ga_3O_7 ceramics with both small *RE* cations (*RE* = Eu, Gd, Tb, Dy, Ho, Y, Er, Tm and Yb) and substantial non-stoichiometries ($Sr_{1-x}RE_{1+x}Ga_3O_{7+x/2}$ with *RE* = Eu, Gd and Tb).[7,26] Some members of the transparent ceramic Sr*RE*Ga_3O_7 family were found to have additional features in their PXRD patterns, implying additional complexity in their crystal structures, but this was not investigated in detail.[7]

Here we investigate the structure and the phase stability of the Sr*RE*Ga_3O_7 (*RE* = Y, Dy, Ho, Er, Tm, Yb and Lu) melilites. In contrast to the modulated Ca*RE*Ga_3O_7 melilites, we find that these materials can crystallize in a new cation-ordered 3 x 1 x 1 melilite superstructure, which produces three distinct A-site environments and enables the large size difference between Sr and the small RE^{3+} cations to be accommodated by the tetrahedral framework. Furthermore, by tuning the synthesis conditions, it is possible to isolate disordered polymorphs for the *RE* = Dy, Ho, Er, Tm and Yb members. The superstructure description is detailed by means of synchrotron and neutron powder diffraction Rietveld refinements, which are coupled to observations from scanning transmission electron microscopy - high angle annular dark field (STEM-HAADF) imaging and X-ray energy dispersive spectroscopy (EDS) elemental mapping. Moreover, atomic-resolution STEM-HAADF imaging and EDS elemental mapping enable direct observation of Sr^{2+} and RE^{3+} cation ordering in the melilite structure. Last, the broad optical transmission range (from the UV up to the mid-infrared) and photoluminescence properties of these new Sr*RE*Ga_3O_7 melilites are measured. A significant influence of the Sr/*RE* ordering/disordering is reported on the *RE* emission band features in the glasses, ordered and disordered ceramics.

2. EXPERIMENTAL

2.1 Synthesis procedure. The small rare-earth compounds Sr*RE*Ga_3O_7 (*RE* = Dy – Lu, Y) and the known tetragonal melilite $SrTbGa_3O_7$ were synthesized by a full crystallization from glass process. First, high purity $SrCO_3$, RE_2O_3 and Ga_2O_3 powders (Strem Chemicals, purity > 99.9 %) were weighed in stoichiometric amounts, and ground together in an agate mortar using ethanol to homogenize the mixture. The resulting powder was then dried, pressed into pellets, and broken into fragments of ~50 mg. The fragments were then levitated individually in an argon gas jet and melted at approximately 1650°C (determined by optical pyrometry) using a pair of CO_2 lasers (10.6 µm),[33] held for several seconds to allow homogenization, and then quenched radiatively to room temperature by shutting off the lasers (an estimated cooling rate of 300°C.s^{-1}) to produce the precursor glasses as spherical beads. Full crystallization of the glass precursors was then achieved by a single heat treatment performed under air in conventional muffle furnace at temperatures between 805-815 °C. Crystallization protocols for each specific composition are detailed in section 3.1.

2.2 Thermal Analysis. Differential scanning calorimetry (DSC) was performed on a Setaram MULTI HTC 1600 instrument. Powder samples of ~200 mg, obtained by crushing several beads of the same composition, were contained in platinum crucibles and scanned at a rate of 10 K min^{-1} in flowing argon.

2.3 Powder Diffraction. Laboratory X-ray powder diffraction (PXRD) analyses were performed in Bragg-Brentano geometry using a D8 Advance Bruker laboratory diffractometer (CuKα radiation) equipped with a LynxEye XE detector. *In situ* high-temperature diffraction data were collected under air using two different setups depending on the maximum temperature required. For measurements up to 1200°C, variable temperature VT-PXRD data were recorded using an HTK1200N Anton Paar furnace. The powder sample was placed in a platinum-lined corundum sample holder. Data were collected from 10 to 40° (2θ) with a 0.024 ° step size and an acquisition time of 1 s/step. Phase transitions were tracked while heating from 740 °C to 900°C for *RE* = Ho-Lu, from 740°C to 1000°C for Dy and from 740°C to 1100°C for Tb, using 5°C steps. Data were also acquired during cooling from the

maximum temperature down to 400°C (300°C for *RE* = Ho). For measurements up to 1600°C, VT-PXRD data were recorded every 50 °C from room temperature up to 1500 °C using an Anton Paar oven chamber (HTK1600N model) from 19 to 38° (2θ) with a 0.016° step size and an acquisition time of 1 s per step. Synchrotron powder diffraction (SPD) was carried out on the 11-BM beamline at the Advanced Photon Source (APS, Argonne National Laboratory, US) for compositions *RE* = Ho, Er, Tm, Yb and Lu. Data were acquired at room temperature from powder loaded in a 0.8 mm diameter Kapton tube with incident wavelength of λ = 0.41423 Å or 0.45787 Å over an angular range of 1 - 50° (2θ) with a step size of 0.001°. Note that the precursor glass powders were scaled up to ~1g for these experiments by combining several crushed beads. Neutron powder diffraction (NPD) data were obtained at the Laboratoire Léon Brillouin (LLB, Saclay, France) on the 3T2 diffractometer at room temperature for *RE* = Yb using an 8 mm diameter vanadium tube. Data were collected with wavelength of λ = 1.229 Å over the 10 - 120° 2θ range with a 0.05° step size, for a total of 22 hours acquisition time. A large (~5g) powder sample was produced for this experiment by crushing a large number of individual beads. Structure refinements were performed from powder diffraction data using TOPAS Academic version 6.[34]

2.4 Electron Diffraction and Imaging. Selected area electron diffraction (SAED) experiments were carried out on a Philips CM20 transmission electron microscope (TEM) to determine the cell parameters and space group of the transparent polycrystalline ceramics. Atomic-resolution STEM-HAADF micrographs and EDS elemental mapping were performed on a JEOL ARM200F (JEOL Ltd.) Cold FEG TEM operating at 200kV, equipped with a double spherical aberration corrector and fitted with a JEOL SDD CENTURIO EDS system. The cationic ordering in $SrYbGa_3O_7$ was imaged at the atomic scale by STEM-EDS elemental mapping and by STEM-HAADF imaging mode with a 68-174.5 mrad inner-outer collection angles. The probe size used is 0.13 nm and 0.1 nm respectively. The samples were first prepared by mechanical polishing with a tripod and inlaid diamond discs until a 50µm thickness. The thin foils were then obtained by argon ion milling (PIPS GATAN).

2.5 Optical Transmission and Photoluminescence Spectroscopies. Optical transmission spectra were recorded on polished samples in the UV-visible-near-infrared (NIR) and infrared ranges using an Agilent Cary 5000 UV-vis-NIR double beam spectrophotometer and a Perkin Elmer Frontier FTIR spectrometer respectively. Photoluminescence spectra were recorded at room temperature on bulk and powder samples using a Horiba-Jobin-Yvon Nanolog spectrofluorimeter, equipped with a 450W Xe lamp source coupled to a double monochromator for excitation, and an iHR320 spectrometer coupled to an infrared PMT detector sensitive from 950 to 1650 nm (Hamamatsu). Special attention was paid to collect the emission spectra under the same experimental conditions to allow their accurate comparison.

3. RESULTS

3.1 Glass-crystallization synthesis of ceramic powders. The precursor glasses prepared by the aerodynamic levitation laser-melting procedure (see section 2.1) were confirmed to be amorphous by PXRD prior to a provisional thermal analysis by DSC conducted on heating up to 920°C. Fully-amorphous samples were obtained for all of the compositions attempted, with the exception of the end member *RE* = Lu, which contained weak Bragg peaks consistent with the presence of a small amount of crystalline melilite (Figure S1). The glass crystallization temperatures, signified by a strong exothermic peak in the DSC, were found to occur in the range 804 – 860°C (see section 3.4); the decrease of the rare-earth size from Tb – Lu induces a systematic increase of the glass transition and crystallization temperatures (associated with increased rigidity of the glass network).[35] Glass powders were finally heat treated for 2 hours at 815°C and cooled down in the furnace (for *RE* = Tb - Yb, Y) or heat treated for 2 hours at 805°C and quenched by placing the Pt crucible in water (for *RE* = Lu) to produce polycrystalline samples.

Laboratory PXRD of these samples showed that two distinct crystal structures had formed, according to the identity of the rare earth ion. For the larger rare-earths (*RE* = Tb, Dy, Ho and Y), the PXRDs were readily indexed to the familiar tetragonal melilite structure ($P\bar{4}2_1m$ with $a \approx 7.9$ and $c \approx 5.2$ Å). However, the smaller rare earths (*RE* = Er, Tm, Yb, Lu) exhibited a more complex PXRD pattern which contained the main reflections of the melilite structure, and an additional set of weak reflections. These patterns were indexed using Dicvol,[36] revealing a three-fold expansion of the melilite unit cell along the *a* axis to produce a new orthorhombic supercell of dimensions ($a \approx 23.70$ Å, $b \approx 7.92$ Å and $c \approx 5.21$ Å). The detailed determination of the 3x1x1 melilite structure by powder crystallography and electron microscopy is described first in sections 3.2 and 3.3. The compositional and thermal stability of

this superstructure, as determined by variable temperature PXRD and DSC measurements, is then described in section 3.4.

Attempts to synthesize the small-rare earth compositions (*RE* = Ho – Lu) directly by classic solid-state reaction were not successful. For example, a variable-temperature PXRD experiment showed that a reaction mixture of $SrCO_3$-Yb_2O_3-Ga_2O_3 produces $SrGa_2O_4$ and $Yb_3Ga_5O_{12}$ as the only ternary phases before melting at 1500°C (Figure S2). As reported by Boyer et al.[7], it is possible to synthesize Sr*RE*Ga_3O_7 transparent ceramics of these compositions by full crystallization from glass (Figure S3a), starting from Sr*RE*Ga_3O_7 glass beads produced as described in section 2.1 and annealing them in a second step: the transparent ceramics thus produced exhibit the same PXRD patterns as for the powder samples described above.

3.2 Solution and refinement of the 3x1x1 superstructure. Sr*RE*Ga_3O_7 synchrotron X-ray diffraction (SPD) and selected area electron diffraction (SAED) patterns were consistent with laboratory PXRD, confirming the presence of a superstructure with a supercell corresponding to a tripling of the *a* axis in a 3x1x1 expansion (Figure 1) of the tetragonal melilite parent cell (Figure S4). The only observed reflection conditions were *h*00, *h* = 2n and 0*k*0, *k* = 2n, consistent with space group $P2_12_12$. Note that we did not see any evidence of satellite peaks in the $SrTmGa_3O_7$ SAED patterns, which implies that the crystal structure is commensurate (in contrast to small-alkaline-earth melilites such as $CaLaGa_3O_7$ and $CaNdGa_3O_7$ which exhibit incommensurate structural distortions)[8,12].

We selected $SrYbGa_3O_7$ as a representative sample for detailed structural analysis due to the high stability of the 3x1x1 superstructure at this composition (see section 3.4), and its favorable neutron diffraction characteristics (relatively low neutron absorption by Yb, and good scattering contrast between Yb/Sr). The structure was solved by charge-flipping[37,38] (implemented in JANA2006[39] through the Superflip software[40,41]) followed by Fourier different mapping, as described in the Supporting Information. The final Rietveld analysis was performed against SPD and NPD data simultaneously. Initial refinement of the Sr/Yb occupancies of the A sites produced three distinct A sites with equal multiplicity: a mixed Yb/Sr site ("Yb1/Sr1", refined occupancy 0.498(1)/0.501(1)), a Yb-dominated site "Yb2" (0.977(1)/0.023(1)), and a Sr-dominated site "Sr3" (0.025(2)/0.975(2)). The amount of site inversion being very limited, these values were then fixed to ideal occupancies (0.5/0.5, 1/0 and 0/1 respectively), which did not affect the goodness of fit. All atomic coordinates were then refined in addition to anisotropic thermal parameters (Sr/Yb positions only) or isotropic thermal parameters (Ga and oxide positions) to give reliability factors R_{wp} = 4.427 %, R_p = 3.772 % and χ^2 = 1.035. The Rietveld refinement is presented in Figure 2, Table 1 and Table S1, with the principal interatomic distances presented in Table 2 and Table S2.

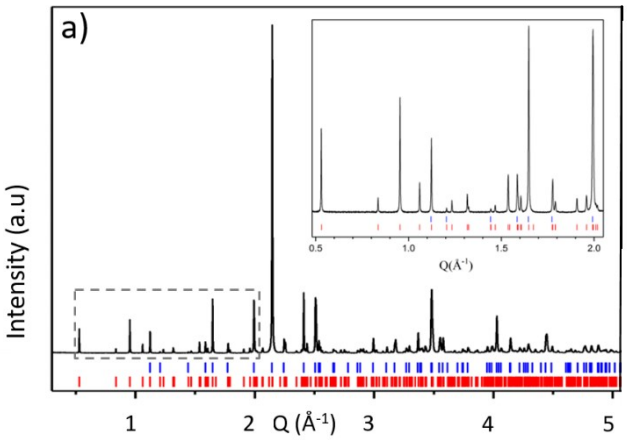

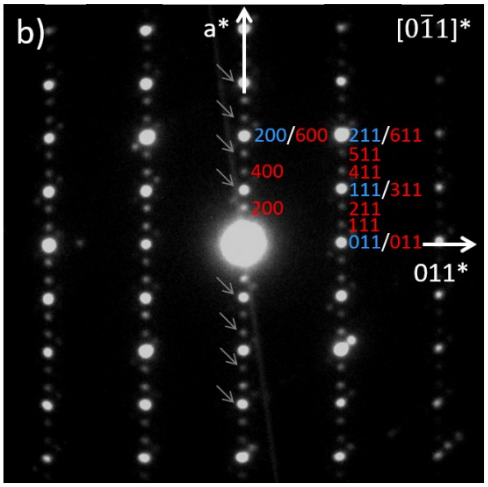

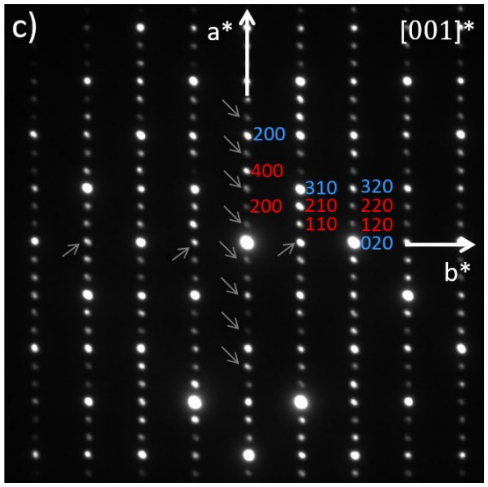

Figure 1. (a) Synchrotron powder diffraction data of the $SrYbGa_3O_7$ melilite phase indexed with the *P*-42$_1$*m* melilite sub-structure (blue marks) and in the 3x1x1 *P*2$_1$2$_1$2 superstructure (red marks). (b) [0-11]* and [001]* Selected Area Electron Diffraction patterns of the $SrTmGa_3O_7$ melilite phase synthesized by full crystallization from glass. The indexations of the tetragonal melilite sub-structure (a=7.9 Å x c = 5.2 Å, *P*-42$_1$*m*) and the 3x1x1 super-structure (a=23.7 Å x b=7.9 Å x c = 5.2 Å, P2$_1$2$_1$2) are shown in blue and red respectively. The arrows point the reflections assigned to double diffraction.

Table 1. Structural parameters of cation-ordered $SrYbGa_3O_7$ obtained by Rietveld refinement against SPD and NPD data (combined) at room temperature (*P*2$_1$2$_1$2 space group, *a* = 23.70167(7) Å, *b* = 7.92110(3) Å and *c* = 5.21162(2) Å).

Atom	Site	x	y	z	Occ	U(eq)
Yb1/Sr1	4c	0.21967(3)	0.14373(8)	0.49426(12)	0.5/0.5	0.0077(2)*
Yb2	4c	0.38103(2)	0.30934(6)	0.45529(9)	1	0.0101(1)*
Sr3	4c	0.05795(4)	0.33953(11)	0.50839(18)	1	0.0098(2)*
Ga1	4c	0.44940(4)	0.14505(14)	0.0131(2)	1	0.0054(3)
Ga2	2a	0	0	0.9759(4)	1	0.0066(4)
Ga3	4c	0.17317(5)	0.48007(13)	0.0014(3)	1	0.0047(2)
Ga4	4c	0.28948(4)	0.33540(13)	0.9535(2)	1	0.0056(3)
Ga5	4c	0.11858(5)	0.12314(12)	0.03036(19)	1	0.0065(3)
O1	4c	0.45607(14)	0.3444(5)	0.2033(7)	1	0.0089(7)
O2	4c	0.38457(14)	0.0730(4)	0.1899(6)	1	0.0043(7)
O3	4c	0.29223(14)	0.3327(5)	0.3001(7)	1	0.0190(10)
O4	4c	0.44114(14)	0.1434(5)	0.6766(6)	1	0.0095(7)
O5	4c	0.12726(17)	0.1121(5)	0.6862(6)	1	0.0150(8)
O6	2b	0.5	0	0.1551(9)	1	0.0082(10)
O7	4c	0.22859(17)	0.4269(5)	0.7736(8)	1	0.0156(8)
O8	4c	0.04632(15)	0.1439(5)	0.1532(7)	1	0.0167(9)
O9	4c	0.29646(16)	0.1315(6)	0.7764(8)	1	0.0173(9)
O10	4c	0.15349(17)	0.2993(5)	0.2025(7)	1	0.0170(9)
O11	4c	0.34815(14)	0.4525(4)	0.7940(6)	1	0.0079(7)

*: The thermal parameters of Yb1/Sr1, Yb2 and Sr3 were refined as anisotropic (see details in table S1).

Table 2. *A*-O interatomic distances and bond valence sums calculated for the three crystallographic A-sites of cation-ordered $SrYbGa_3O_7$.

Bond	Length(Å)	Bond	Length(Å)	Bond	Length(Å)
(Sr/Yb)1-O9	2.342(4)	Yb2-O1	2.228(3)	Sr3-O8	2.430(4)
(Sr/Yb)1-O5	2.421(4)	Yb2-O11	2.238(3)	Sr3-O6	2.565(3)
(Sr/Yb)1-O3	2.494(4)	Yb2-O4	2.256(4)	Sr3-O4	2.593(4)
(Sr/Yb)1-O10	2.508(4)	Yb2-O3	2.262(3)	Sr3-O5	2.608(4)
(Sr/Yb)1-O7	2.531(4)	Yb2-O2	2.329(3)	Sr3-O2	2.783(3)
(Sr/Yb)1-O11	2.671(3)	Yb2-O5	2.517(4)	Sr3-O10	2.788(4)
(Sr/Yb)1-O7	2.682(4)	Yb2-O9	2.967(4)	Sr3-O4	2.935(3)
(Sr/Yb)1-O3	2.702(4)	Yb2-O11	3.711(3)	Sr3-O1	3.195(4)
BVS (Sr)	2.68	BVS (Sr)	3.84	BVS (Sr)	1.76
BVS (Yb)	1.87	BVS (Yb)	2.68	BVS (Yb)	1.23

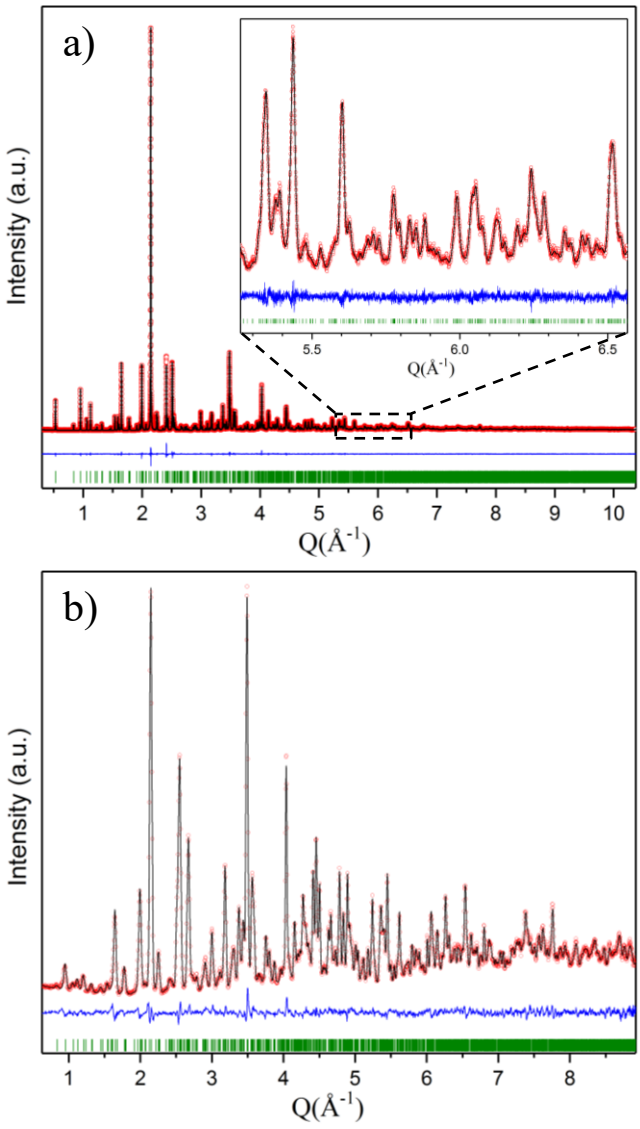

Figure 2. Combined Rietveld refinement of SPD (a) and NPD (b) data on cation-ordered $SrYbGa_3O_7$ melilite at room temperature (R_p = 3.772% R_{wp} = 4.427%). Observed (red points), calculated (black line) and difference (blue line) profiles are shown. The green tick marks correspond to allowed reflection positions.

The refined $SrYbGa_3O_7$ melilite superstructure is presented in Figure 3. Its crystal structure retains the topology of the parent melilite structure, where corner-sharing GaO_4 tetrahedra form two dimensional Ga_3O_7 sheets with the A cations accommodated in pentagonal channels that align parallel to the stacking axis. In the tetragonal parent structure (e.g. the structure of $SrLaGa_3O_7$, shown in Figure 3b), the Sr/La site cations are fully disordered and the channels are symmetrically equivalent with 8 nearest-neighbor A-O distances in the range 2.51 – 2.94 Å[6,42]. In contrast, in $SrYbGa_3O_7$ the ordering of large/small A site cations (8-coordinate ionic radii of 1.25 and 0.985 Å for Sr^{2+} and Yb^{3+} respectively) over three different sites causes the Ga_3O_7 framework to distort (Figure 3a). This produces three distinct channel types which have equal multiplicity.

The A sites in the Sr-containing channels Yb1/Sr1 (half-occupied by Sr^{2+}) and Sr3 (fully-occupied by Sr^{2+}) can be considered as distorted versions of the 8-coordinate square-antiprismatic A-sites found in the parent melilite $SrLaGa_3O_7$ (Figure 3d and e). In the Sr3 channels, the bond valence sum (BVS) for Sr^{2+} is 1.76, which is comparable to that found in the undistorted $SrLaGa_3O_7$ (BVS = 2.04), despite its broad distribution of Sr-O distances in the range 2.430(4) – 3.195(4) Å (Figure 3e). It is clear that Yb^{3+} would be severely under-bonded at this site (BVS for Yb^{3+} = 1.23). The Yb1/Sr1 sites have A-O distances clustered neatly in the range 2.342(4) – 2.702(4) Å (Figure 3d). These sites retain a formal coordination number of 8, but are smaller than the Sr3 sites, and smaller than the A-sites of $SrLaGa_3O_7$. Here, the calculated BVS values indicate a compromise between the bonding preferences of Sr^{2+} (which is formally over-bonded, with BVS = 2.68) and Yb^{3+} (formally under-bonded, with BVS = 1.87). Such values are comparable with those found in the previously published structure of disordered $SrYGa_3O_7$ (where BVS for Sr^{2+} = 2.37; Y^{3+} = 1.81)[6]. In contrast to the Sr3 and Yb1/Sr1 sites, the Yb2 sites (fully-occupied by Yb^{3+}) are substantially different to those found in $SrLaGa_3O_7$ and can be considered to have [6+1] coordination defined by six short Yb-O distances in the range 2.228(4) – 2.517(4) Å that form a triangular-prismatic first coordination sphere, and one long Yb-O distance of 2.967(4). Note that the next-shortest Yb2-O distance is 3.711(3) Å (Yb2-O11), which is beyond the range usually considered for bonding. This site is small enough to accommodate Yb^{3+} with a BVS of 2.68, whereas coordination of Sr^{2+} would be disfavored (BVS for Sr^{2+} = 3.84). The six short Yb-O distances cause a severe narrowing of the pentagonal channel, as shown by the deviation of its geometry from the ideal case of $SrLaGa_3O_7$ (Figure 3c). The refined A-O distances for all three sites are shown in Table 2. The relationship between the arrangement of the A sites in two dimensions and the corresponding framework distortion is discussed in more detail in section 4.1.

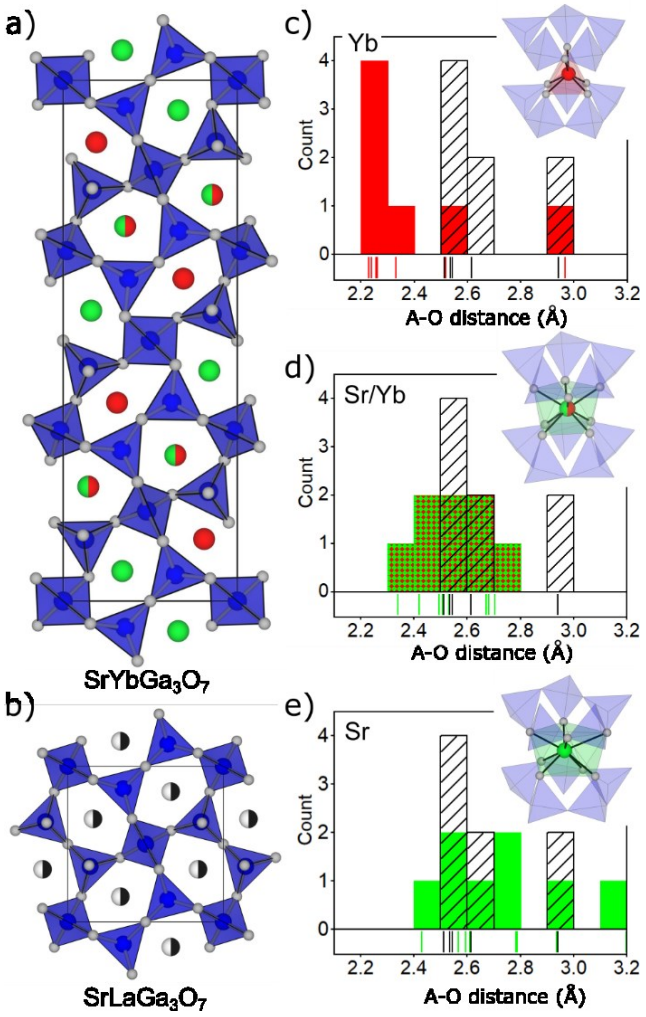

Figure 3. [001] projections of (a) the cation-ordered 3x1x1 melilite superstructure of $SrYbGa_3O_7$, with GaO_4 tetrahedra in blue, Sr in green and Yb in red. (b) the parent melilite structure of $SrLaGa_3O_7$, with the disordered Sr/La site in black/white. (c-e) histograms showing the distribution of refined A-O distances in $SrYbGa_3O_7$ for Yb (red), Sr/Yb (patterned green/red) and Sr (green) sites. Each histogram is overlaid with the published A-O distances of the undistorted $SrLaGa_3O_7$ parent phase (patterned black/white bars).

3.3 Atomic-scale imaging of the 3x1x1 superstructure (*RE* = Yb). The Rietveld refinements of $SrYbGa_3O_7$ provide an average structural model describing the superstructure with three distinct crystallographic A sites (one fully occupied by Yb, one fully occupied by Sr and one shared equally by Sr and Yb), but it may not provide an accurate picture of the local Yb/Sr distribution at the nanometer scale. To investigate the possibility of local deviation in the Yb/Sr distribution (e.g. the presence of areas enriched in Yb or Sr), EDS mapping and STEM-HAADF imaging were performed at the atomic scale, on the $SrYbGa_3O_7$ sample oriented along the [001] direction (Figure 4a and Figure 5). Along this direction, the columns of atoms are composed of the same crystallographic A site (Yb1/Sr1 with a 50/50 occupancy or Yb2 as fully occupied by Yb or Sr3 as fully occupied by Sr), (Figure 3a).

STEM-EDS elemental mapping of the three cations, Ga, Sr and Yb, at the atomic scale (where each point corresponds to a column of atoms with the same chemical nature) shows GaO sites (blue), pure Yb2 sites (red), pure Sr3 sites (green) and mixed Yb1/Sr1 sites highlighted by yellow arrows (Figure 5). This result confirms and allows the cationic organization proposed by powder diffraction to be visualized.

Scanning transmission electron microscopy - high angle annular dark field (STEM-HAADF) is a Z-contrast imaging mode whose signal is essentially dominated by Rutherford scattering, with a cross-section proportional to Z^2 (Z being the atomic number).[43–45] For thin objects (several tens of nanometers), an analytical expression of the Z dependence of the image intensity can be approximated by an exponential function of the form $I \propto Z^n$ with n in the range between 1.6 and 2, depending on the annular dark field (ADF) detector geometry (collection angle). At the atomic scale, for a column composed of several elements (i) with a ratio m_i and Z_i the atomic number of the element i, this formula becomes $I \propto \sum_i (m_i Z_i^n)$. Consequently, one of the advantages of this imaging mode is the possibility to distinguish between chemically different atomic column sites. However, the intensities are highly sensitive to the number of atoms in the atomic column. Considering this point, atomic resolution STEM-HAADF images have been acquired with a $SrYbGa_3O_7$ crystal oriented along the [001] direction in order to stack the same number of atoms along all the atomic columns, whatever their chemical nature (Figure 4a). The cation ordering was then determined by indexing the atomic columns from the brightest to the darkest contrasts in relation with the heaviest sites to the lightest atoms: Yb2 (Z = 70) > Yb1/Sr1 50:50 mixed ($\bar{Z} \approx 56$) > GaO ($\bar{Z} = 39$) ≈ Sr3 (Z = 38). Only the Sr and GaO atomic columns are difficult to distinguish accurately due to their very close atomic numbers. However, by comparison with the EDS elemental maps (Figure 5) and the embedded simulated STEM-HAADF image (top right corner of Figure 4a), all the crystalline sites are identified. The simulated STEM-HAADF image of the $SrYbGa_3O_7$ superstructure, oriented along the [001] zone axis, was obtained using the JEMS software[46] from the cif file of the superstructure. It is a simple projection of the structure convolved with the electron probe intensity of the microscope. The channeling effects have not been simulated. A perfect match in terms of distances and positions between the experimental

STEM-HAADF images and the melilite structure resolved from synchrotron and neutron powder diffraction experiments was found with no sign of modulation or default in the crystallographic site organization.

Recent works[47,48] have demonstrated that a quantification of the total intensity of the scattered electrons (V) for individual atomic columns can enable the nature of unknown columns to be assigned via the formula $V \approx \sum_i (m_i Z_i^n)$ with $n \approx 2$ and m_i the weighting of the different elements i composing the atomic column. This formula has been employed to determine the local Yb1/Sr1 distribution over the mixed site, *i.e.* the deviation around the ideal average 50/50 value determined from powder diffraction. Multiple factors such as thickness variation, the level of noise and channeling can affect the signal. To limit these artefacts, the intensity profiles were extracted for each projected position from the same STEM-HAADF image, assuming the thickness of the sample almost constant through the image (8 nm x 6 nm), as well as the different factors affecting the signal. The signal obtained for each atomic column was fitted with a background signal and a Gaussian function determined for each type of crystallographic site (Sr3, Yb2, Yb1/Sr1) (Figure 4b).[49] The chemical composition of atomic columns of the same crystallographic site (Sr3, Yb2, Yb1/Sr1) can be compared to each other by looking at the corresponding volumes under the peaks which are proportional to the total intensity of electrons scattered toward the ADF detector. According to the formula $V \approx \sum_i (m_i Z_i^n)$ with V the volume under the peak and Z the atomic number of the site, the factor n has been determined for each crystallographic site considering the mixed Yb1/Sr1 site with an average 50/50 occupancy. The n values obtained for the sites Sr3, Yb1/Sr1 and Yb2 were 2.1, 1.99 and 1.94 respectively, in agreement with the literature that predicts a n factor close to 2. Considering these n values, a Z atomic number has been calculated for each measured atomic column and its distribution is presented on the Figure 4c. The three different crystallographic A sites are well distinguished and their average Z values agree with the occupancies Yb/Sr: 1/0 (Z_{Yb} = 70), 0/1 (Z_{Sr} = 38) and 0.5/0.5 ($\overline{Z_{Yb/Sr}} \approx 56$) respectively. The pure Sr3 and Yb2 crystallographic sites show a small Z distribution (± 13% and ± 7% respectively) which can be linked to deviation due to the different factors previously described which affect the signal. In comparison, the variation of the Z value to the Yb1/Sr1 mixed atomic columns (± 14%) is similar to the pure Sr crystallographic site, corresponding to a low variability of the chemical composition between each mixed Yb1/Sr1atomic columns which represent between 40 to 100 cells along the c axis (i.e. 20 to 50 nm in thickness).

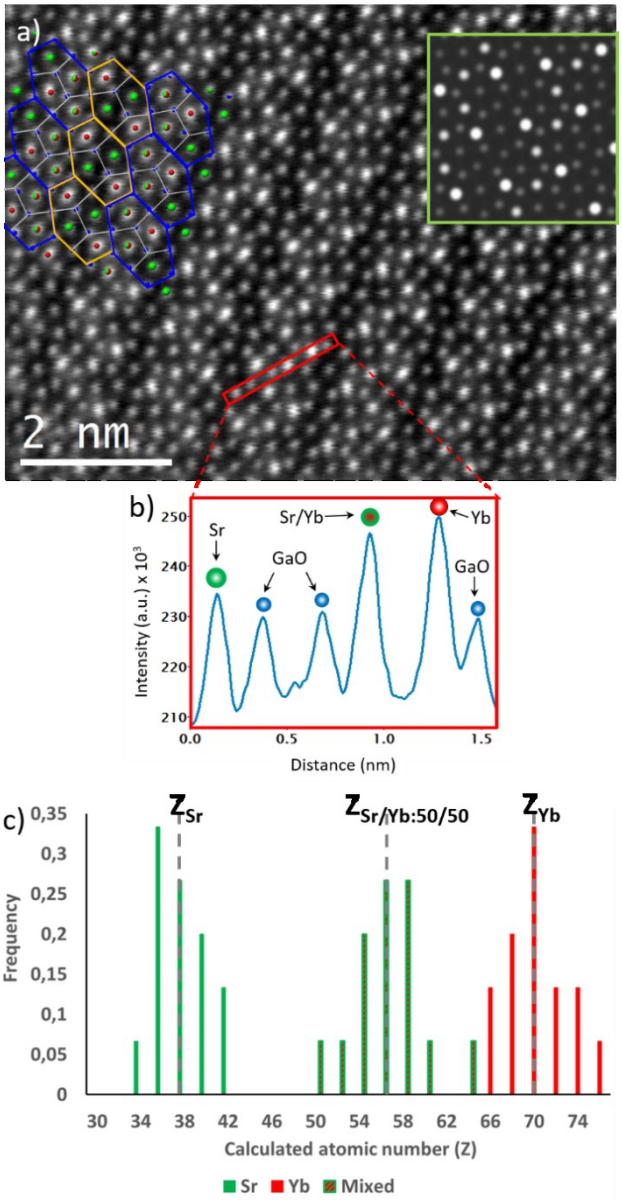

Figure 4. (a) Atomic scale STEM-HAADF micrograph of the $SrYbGa_3O_7$ superstructure sample oriented along the [001] zone axis. The hexagonal ABA' tiling, from the discussion in Section 4.1, is overlaid to highlight the superstructure (Ga, Yb1/Sr1, Yb2 and Sr3 atoms are respectively represented in blue, red, green/red and green). The green framed inset corresponds to a STEM-HAADF simulated image by JEMS software. (b) Experimental profile corresponding to the red framed box area. (c) Distribution of the calculated atomic number (Z) from the measured peak volumes for each crystallographic site (Yb1/Sr1, Yb2 and Sr3).

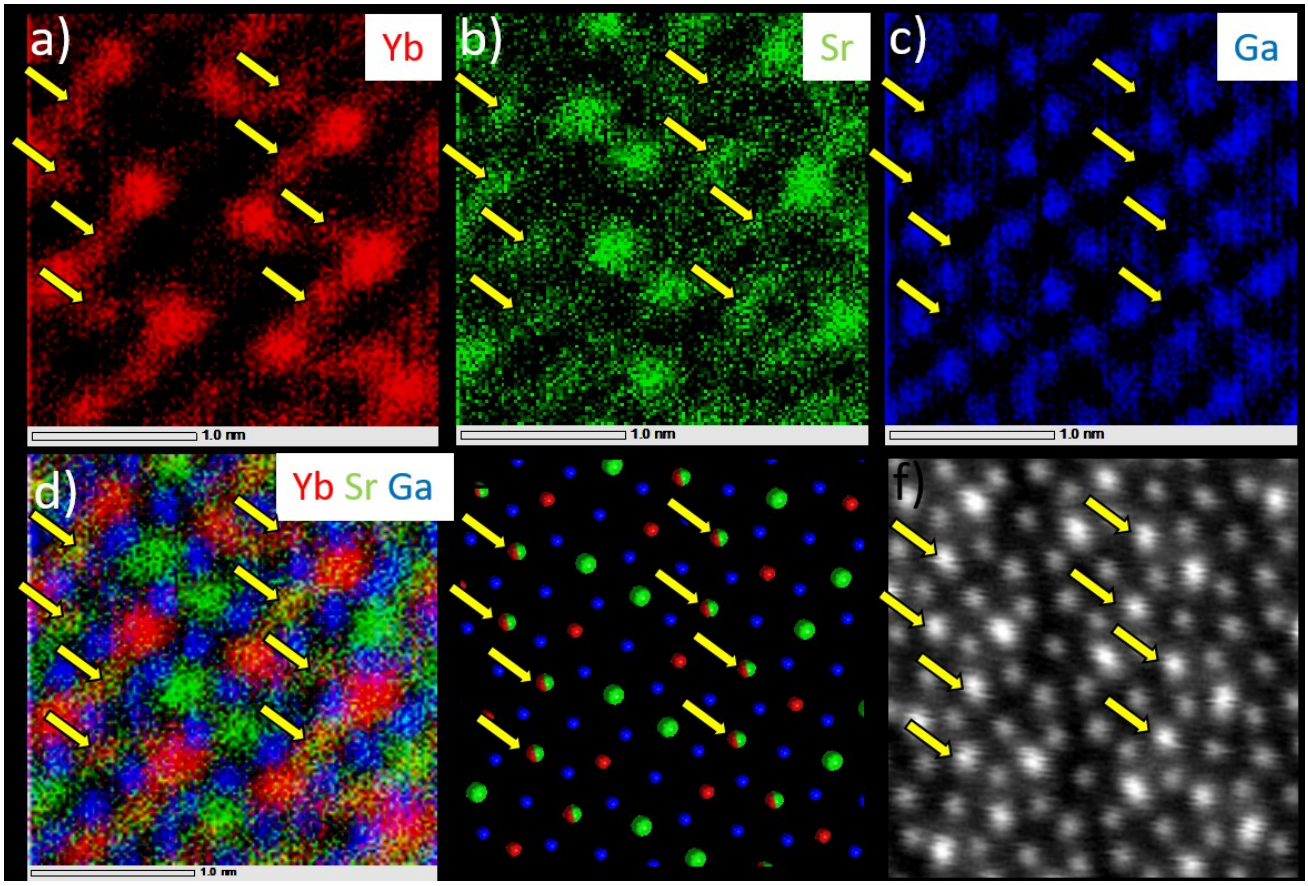

Figure 5. Atomic-scale STEM-EDS elemental maps of the cations (a) Yb (red), (b) Sr (green), (c) Ga (blue) and (d) the overlaid EDS maps showing the mixed sites (50/50 Yb1/Sr1) in red/green highlighted by yellow arrows. (e) $SrYbGa_3O_7$ superstructure projection of the cationic sites along the [001] axis. Ga atoms are drawn in blue, Sr3 sites in green, Yb2 sites in red and the mixed sites (50/50 Yb1/Sr1) in red/green. (f) STEM-HAADF image of the $SrYbGa_3O_7$ superstructure along the [001] zone axis. On all the images the yellow arrows highlight the mixed Yb1/Sr1 sites (50/50 average occupancy).

3.4 Thermal stability and structural phase diagram across the series *RE* = Tb – Lu, Y. The occurrence of the 3x1x1 superstructure as a function of composition (*RE* = Tb-Lu, Y) and temperature were mapped by a combination of *in situ* high temperature PXRD and thermal analysis by DSC. The PXRD experiments started from precursor glasses, which were heated in 5°C steps from 740°C, until the point where thermal decomposition of the melilite into binary (RE_2O_3) and ternary (garnet-type) oxides was observed. This was then followed by measurements on cooling to room temperature, as shown in Figure 6. A measurement time of 30 min.step^{-1} was used to ensure the reliable detection of low-intensity superstructure peaks, resulting in an average heating rate of approximately 0.17°C min^{-1}. The *RE* = Lu member was found to have the lowest thermal stability with decomposition products appearing at 830°C, which is only ~50°C higher than its glass crystallization temperature, and this was the only sample to decompose substantially during the measurement. The *RE* = Ho, Er, Tm and Yb members were found to have higher decomposition temperatures in the range 850 – 870°C. This, together with their lower glass-crystallization temperatures, means that a wider temperature window is available for their synthesis. Members with rare-earths larger than Ho were found to be the most stable with respect to decomposition: *RE* = Y, Dy and Tb were found to decompose at 890°C, 965°C and 1010°C respectively. For comparison, *RE* = Gd is not susceptible to thermal decomposition, as demonstrated by successful melt-growths of single crystals.[50] This indicates that the boundary of the metastable small-rare-earth melilites lies between *RE* = Gd and Tb (see Figure 8).

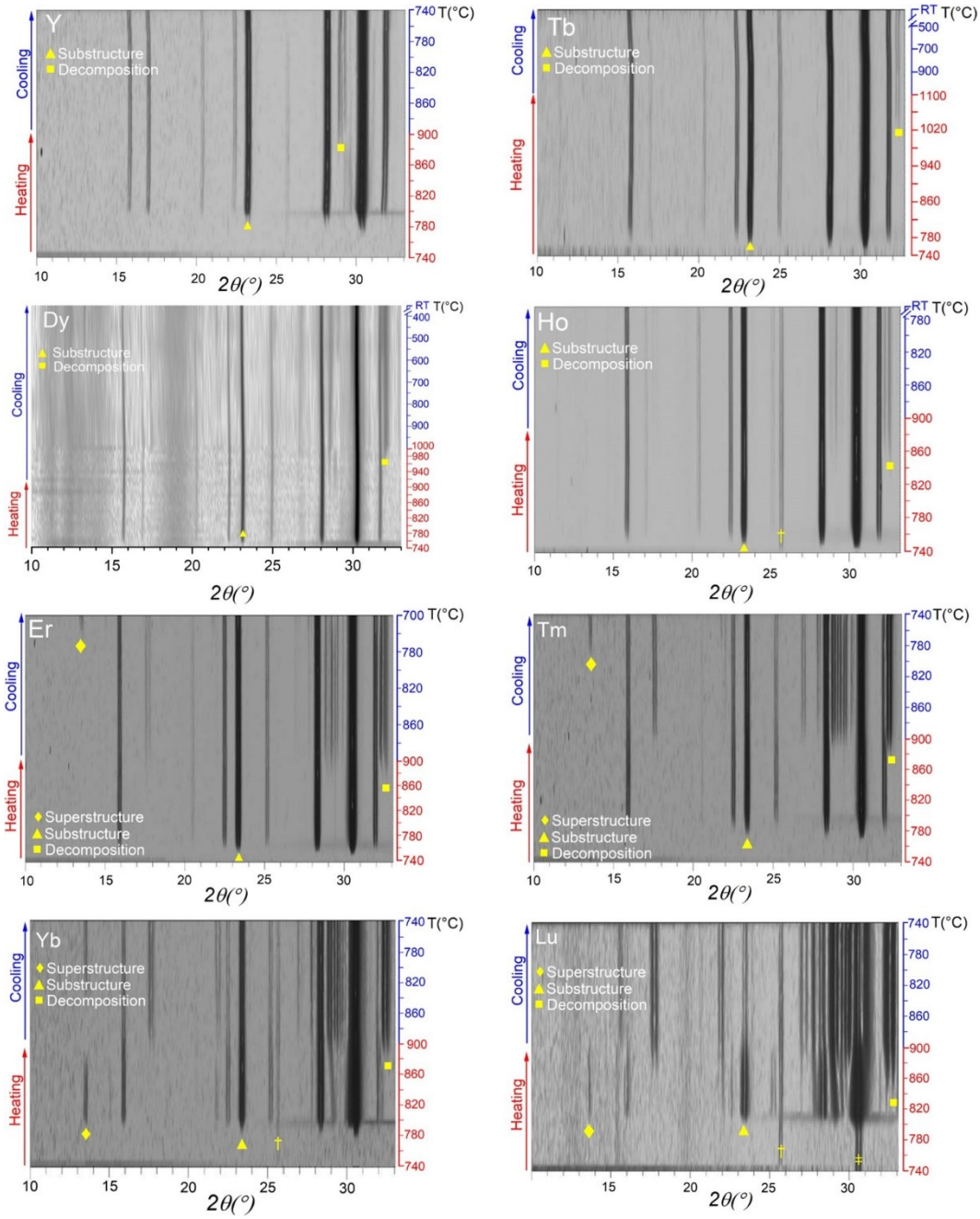

Figure 6. Variable temperature powder X-Ray diffraction (VT-PXRD) on Sr*RE*Ga_3O_7 (RE= Tb – Lu, Y) on heating and cooling, starting from the precursor glasses. Peaks representing the initial melilite (substructure) crystallization, the 3x1x1 structural ordering (superstructure), and the onset of decomposition are indicated respectively by triangle, diamond and square symbols. Note that the maximum intensities of the decomposition peaks are between 1-3% (Tb, Dy, Ho, Er, Y) or 5-8% (Tm, Yb) of the most-intense melilite peak, whilst Lu decomposed substantially (~50%). Peaks labelled † arise from the alumina sample holder. The precursor glass for *RE* = Lu contained a small amount of crystallized melilite, indicated by ǂ.

The onset temperatures of the parent (A-site disordered) tetragonal melilite and 3x1x1 superstructure peaks revealed three categories of behavior that depend on the size of the rare earth cation. (i) The smallest *RE* members (*RE* = Yb and Lu) were found to crystallize directly into the 3x1x1 melilite superstructure upon heating. In these compounds, the superstructure was retained throughout the experiment on cooling to room temperature. (ii) The intermediate-*RE* members (*RE* = Er and Tm) crystallized first into the parent melilite structure, which was then retained up to high temperature. However, on cooling below 720°C and 790°C respectively, they transformed into the 3x1x1 superstructure which was then retained all the way to room temperature. (iii) The largest *RE* members (*RE* = Tb, Dy, Y and Ho) crystallized into the parent melilite structure, and retained this structure throughout the experiment. Note that, in all cases, the products obtained at room temperature were consistent with the results of *ex situ* crystallization described in section 3.1.

The DSC scans, measured in parallel with the *in situ* PXRD over the range 25 – 925°C, used a constant temperature scan rate of 10°C min^{-1} on heating and cooling (Figure 7), substantially faster that the average rate of the *in-situ* PXRD experiments. The DSC data collected on heating are dominated by the strong exothermic peaks from glass crystallization in the range 804°C (*RE* = Tb) to 858°C (*RE* = Lu), as shown in Figure 7a. However, with the exception of the end-members (*RE* = Tb and Lu), the cooling curves were found to exhibit a small exothermic peak whose position varied systematically with composition, as shown in Figure 7b. The onset temperatures of these peaks are strongly correlated with the identity of the *RE* cation: a maximum of 853°C was observed for *RE* = Yb, with a near-monotonic decrease to 548°C for *RE* = Dy. For Er and Tm, their peaks at 713°C and 800°C respectively agree closely with the superstructure ordering temperatures observed on cooling *in situ* by PXRD. Post-measurement *ex-situ* PXRD scans showed that all of these samples, with the exception of *RE* = Tb (which showed no exothermic peak on cooling), had crystallized in the 3x1x1 superstructure (Figure S5). The exothermic event observed on cooling thus corresponds to a structural phase transition from the tetragonal parent melilite structure to the orthorhombic 3x1x1 melilite superstructure.

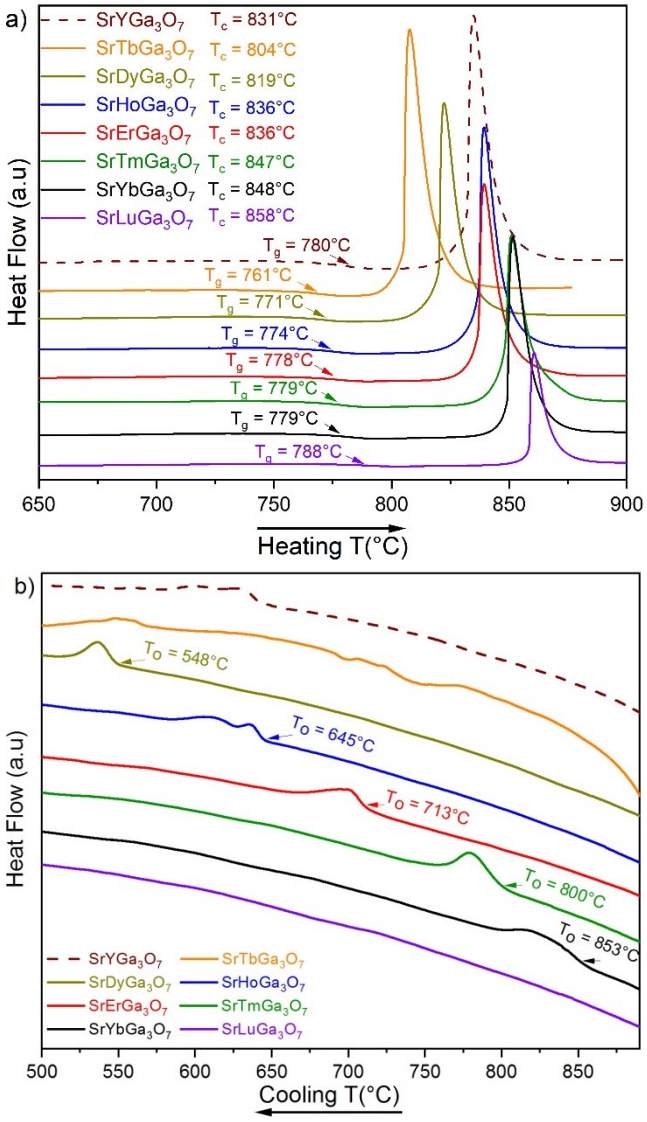

Figure 7. Differential Scanning Calorimetry (DSC) measurements of Sr*RE*Ga3O7 (*RE* = Tb – Lu, Y) glass composition, where Tg, Tc and To are glass transition, crystallization and ordering temperatures respectively. a) Heating plots using a 10°C/min heating rates from room temperatures to 925°C, b) Cooling plots using a 10°C/min cooling rates from 925°C to room temperatures.

These thermal analysis results demonstrate that the 3 x 1 x 1 superstructure can be formed for the larger rare-earth members *RE* = Dy, Y and Ho if they are crystallized with appropriate heating and cooling rates (Figure S6). Furthermore, they suggest that it should be possible to recover the parent tetragonal polymorphs of the intermediate- and small-*RE* members (Er – Yb) at room temperature by rapid cooling from the disordered domain (Figure S6). To test this, we used a conventional muffle furnace to heat powdered precursor glasses of each composition (*RE* = Er, Tm and Yb) in a platinum crucible at 10°C min^{-1} to ~50°C above their transition temperatures T_O (defined by the exothermic

peak in the DSC cooling scan), and then immediately quenched them to room temperature by removing them from the furnace. PXRD confirmed that the tetragonal parent melilite structure had been isolated for each of these compositions (Figure S7, S8). Attempts to quench $SrLuGa_3O_7$ in this way, from ~10°C below its decomposition temperature, only produced the 3x1x1 superstructure. This is consistent with the absence of a phase transition peak in the DSC cooling scan of this compound: our results indicate that this structure is cation-ordered through its entire stability range.

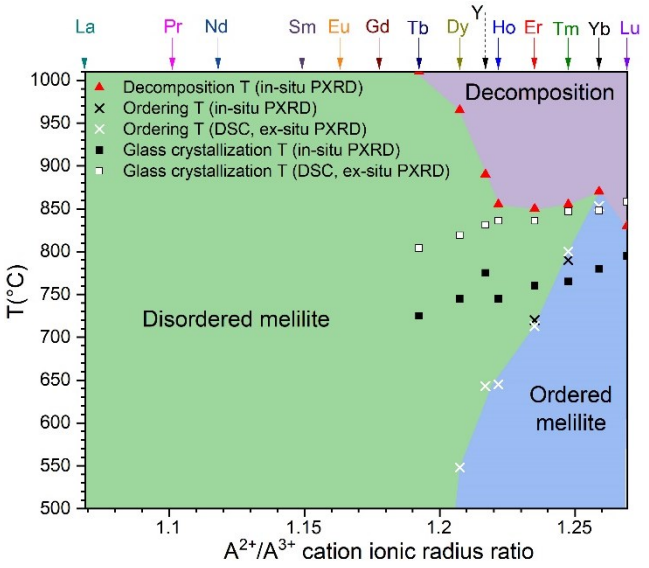

Figure 8. Sr*RE*Ga_3O_7 phase diagram showing the maximum extent of the 3x1x1 superstructure domain, as a function of temperature and A-site ionic radius ratio. The points for *RE* = Tb – Lu, Y are drawn from DSC and VT-PXRD results (this work), whilst the region *RE* = La – Gd is drawn from the literature[49].

3.5 Structural trends across the series *RE* = Dy – Lu, Y. The structural model derived for $SrYbGa_3O_7$ was used as a template for Rietveld refinement of the 3x1x1 superstructure polymorphs of *RE* = Ho, Er, Tm and Lu (using SPD data) and *RE* = Dy (using laboratory PXRD) (Figure S9-S12). For *RE* = Ho, Er and Tm the lattice parameters, atomic positions, and isotropic thermal parameters were refined (with all oxygen atoms assigned the same thermal parameter) (Table S3-S12), and the fractional occupancies of Sr and *RE* on the three A sites were refined with a global compositional constraint to match the nominal stoichiometry. This produced good fits to the data for all compositions (for structural parameters and agreement factors see table S3-S8 and figure S10, S11). These refinements all revealed a partitioning of Sr and *RE* over the three A sites that is consistent with the structure of $SrYbGa_3O_7$. Like $SrYbGa_3O_7$, the next-smallest member $SrTmGa_3O_7$ was found to exhibit complete cation ordering on the A sites, whilst refinements of the larger *RE* = Dy – Er members revealed a small amount of disorder between the *RE*2 and Sr3 sites. This can be seen most clearly for $SrErGa_3O_7$, where Er occupancy refined to 0.50 for RE1/Sr1, 0.866(3) for RE2, and 0.130(4) for Sr3. These structures are still strongly cation-ordered, but these small deviations from the $SrYbGa_3O_7$ model are consistent with the weakening stability of the 3x1x1 superstructure as the *RE* radius increases (sections 3.4 and 4.2). It is possible that this apparent partial Sr/*RE* site inversion, indicated by the Rietveld refinements, actually corresponds to the presence of fully-disordered microstructural domains in these samples: this appears to be the case for *RE* = Y, where HRTEM imaging and associated FFTs show clearly, in a single grain, the coexistence of ordered and disordered nanodomains of size 20-30 nm with the same [001]* orientation (Figure S13), suggesting that disorder is introduced at the nanometer scale, rather than at unit cell scale. The possible existence of such ordered/disordered domains in the *RE* = Dy – Er members provides an alternative explanation for the partial disorder over the *RE*2 and Sr3 sites which is apparent in their refined (average) structures.

The SPD data revealed $SrLuGa_3O_7$ to have a lower crystallinity than the other members with significantly broader Bragg peaks, consistent with its high glass-crystallization temperature and small thermal stability window. For this composition only, deviations of the Ga-O distances from their corresponding values in $SrYbGa_3O_7$ were restrained by a penalty function in order to obtain a physically plausible model. Additionally, it was necessary to split the Lu3 site to avoid an unphysically large thermal parameter at this site. Although this produced a satisfactory fit to the SPD data (R_{wp} = 9.18 %, R_p = 6.87 %, see Table S9), these factors render the *RE* = Lu model less precise than those of the other highly-crystalline *RE* members, and may indicate complex local disorder in this sample.

The disordered polymorphs, which were synthesized for *RE* = Dy – Yb by quenching from high temperatures (see section 3.4), have ionic radius ratios of the A (Sr/*RE*) and B (Ga) cations that lie close to the incommensurately-ordered structural domain proposed by Wei *et. al.*[8,12] for the small alkaline-earth melilites Ca*RE*Ga_3O_7. To test this possibility, we conducted SAED measurements on disordered $SrTmGa_3O_7$ (Figure S4), which confirmed the tetragonal $P\text{-}42_1m$ indexation and contained no evidence of incommensurate satellite reflections. We then proceeded with Rietveld

analysis using laboratory PXRD data with the tetragonal $P\text{-}42_1m$ model of the parent melilite $SrLaGa_3O_7$ as a structural template (Figure S10, S11). Unit cell parameters and atomic coordinates were refined with no additional constraints. Across the series, the trend in lattice parameters follows the expected lanthanide contraction and is consistent with the trend observed in the superstructured polymorphs (see normalized lattice parameters, Figure S14 and Table S13, S15, S17, S19). The mean Sr/*RE*-O distances were found to lie in the range 2.590(8) – 2.600(5) Å, which is consistent with the parent $SrLaGa_3O_7$ melilite (mean Sr/La-O 2.655 Å) (Table S14, S16, S18 and S20).

3.6 Optical properties. The optical transmission spectra in the UV-vis-NIR range (200 to 2700 nm) of the $SrREGa_3O_7$ glasses and ceramics have been already reported in anterior works[7]. Optical transparency of both glasses and ceramics actually spans from ~300 nm up to ~7 µm (at an arbitrary transmittance value of 10% for 1 mm thick samples), as can be seen in and confirmed by the transmission windows presented in Figure S15. Optical scattering losses can be observed on all the ceramics in the short-wavelength region of their transmission spectra, as expected. Maximum transmission also drops from 80% for the glasses down to 40-60% for the ceramics, excepted for the $SrYbGa_3O_7$ ceramic which maintains above 70% of transmission in the mid-infrared range. Moreover, a clear structuration (narrower band width and sharper peak intensity) of the absorption bands characteristic to the *RE* cations is also noticed: around 1480-1530 nm for the Er^{3+} ion, 1900-2000 nm for the Ho^{3+} ion, 1600-1800 nm for the Tm^{3+} ion and 975 nm for the Yb^{3+} ion, for instance (Figure S16). This confirms the structural environment ordering around the *RE* cation induced during the full crystallization from the glass. To better evidence this influence, emission photoluminescence spectroscopic measurements were focused on the $SrErGa_3O_7$ melilites. The fluorescence spectroscopy of the Er^{3+} ion is indeed well-known and exploited in numerous applications (e.g. in optical fiber amplifier for telecommunications). The emission spectra recorded in the 1400-1650 nm region under excitation at 520 nm on glass and ceramic melilite bulks reveal a strong enhancement of the emission intensity in the ceramic material (Figure S17). Besides, one can observe a raising of several structured peaks along the Er^{3+} broad emission band in the ceramic, resulting from the more defined structural ordering around the Er^{3+} ions.

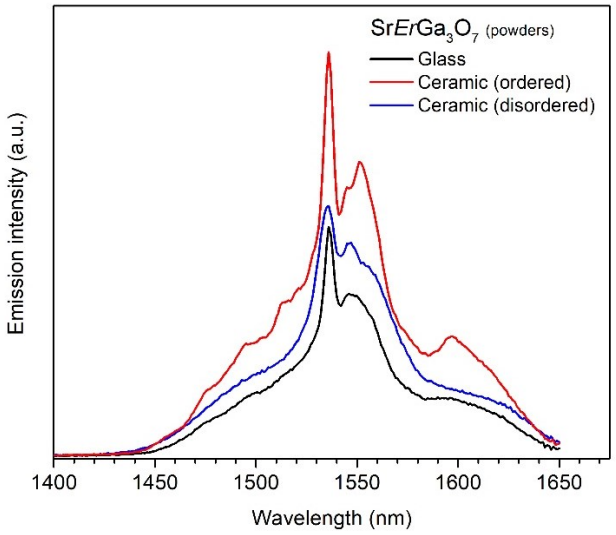

Figure 9. Near infrared emission band of the $SrErGa_3O_7$ glass, ordered and disordered ceramics powdered samples, under excitation at 520 nm (Xe lamp source). Data were collected in the strictly same conditions.

Photoluminescence emission spectra have been also recorded on the $SrErGa_3O_7$ glass, ordered and disordered ceramic powdered samples, as presented in Figure 9. Strictly the same experimental conditions and amounts of finely crushed powders were employed to enable accurate comparison of their emission spectrum. In comparison with the emission spectra recorded on bulk polished samples (Figure S17), no significant difference of emission intensity is noticed here between the glass and ceramics emission band. Then, one can also notice a stronger structuration of the band in the ordered ceramic *vs* the disordered ceramic, whose band shape is very similar to that recorded in the glass.

DISCUSSION

4.1 Origin of the 3x1x1 superstructure. Whilst the preference of the large (Sr) and small (*RE*) cations for different coordination sites explains the occurrence and relative stabilities of the ordered and disordered structures in this series (see section 4.2), it does not explain why the 3x1x1 superstructure retains a substantial degree of disorder; *i.e.* why Sr and *RE* are ordered over three different sites (Sr-only, *RE*-only and mixed), instead of segregating completely over two sites (Sr-only and *RE*-only) which would give a fully-ordered structure. This can be considered by expanding the view of the 3x1x1 superstructure (Figure 10) to reveal the full complexity of the cation ordering. The most striking feature is that the small highly-distorted *RE*2 sites, populated exclusively by *RE*, are arranged in two dimensions on a pseudo-hexagonal sublattice which

maximizes their separation (Figure 10a). This arrangement means that the highly distorted pentagonal channels that host them are not required to share edges with each other. In contrast, the larger Sr and Sr/*RE*1 sites are not arranged pseudo-hexagonally, and instead form one-dimensional stripe-like sublattices parallel to the *b* axis.

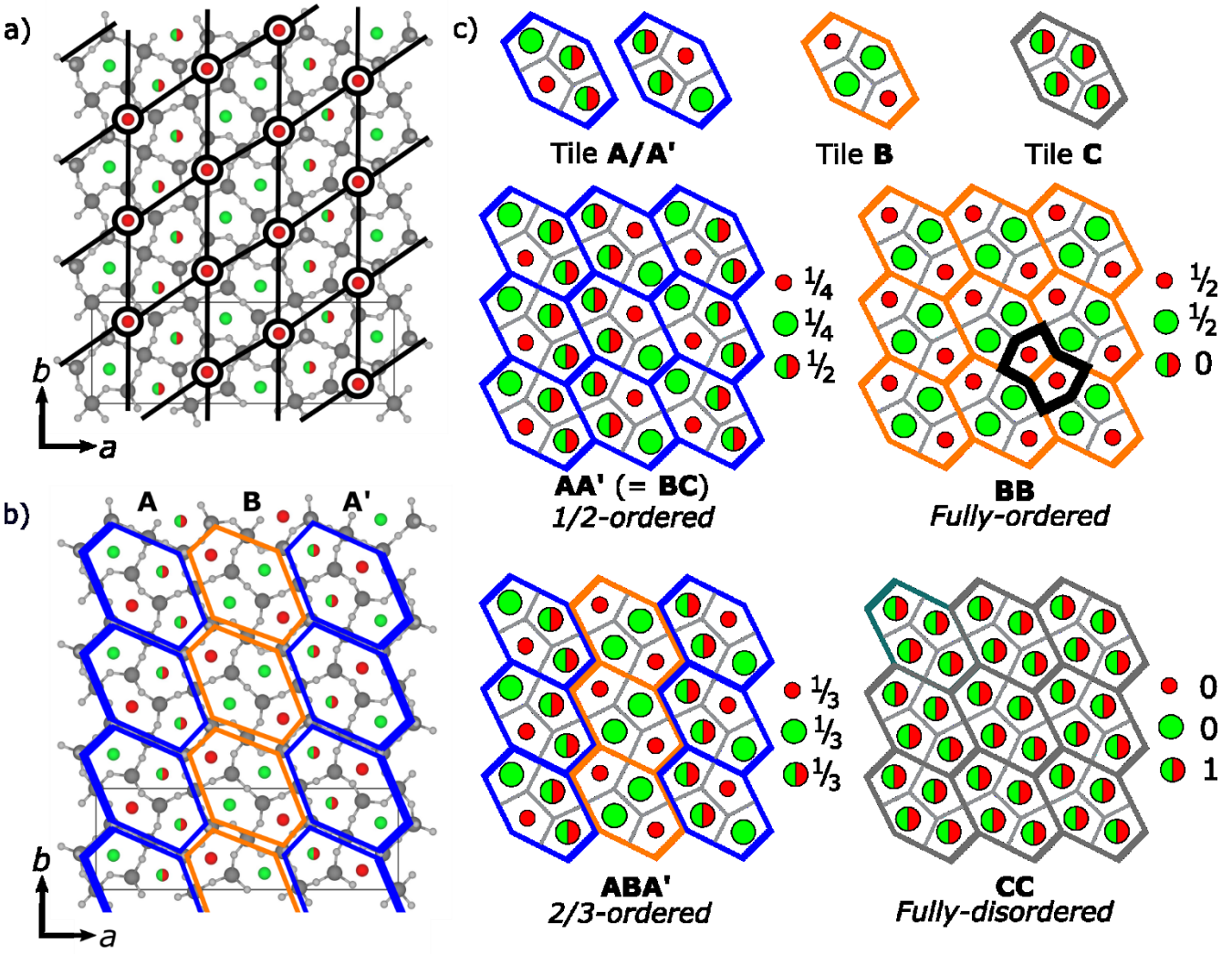

Figure 10. Long-range structural ordering in $SrYbGa_3O_7$. (a) The experimentally-observed arrangement of *RE*2 sites on a pseudo-hexagonal sublattice which maximizes their separation. (b) The experimentally-observed structure viewed as a hexagonal tiling with two tile types in a striped **ABA'** arrangement. (c) The tiles **A**, **B**, **C** can be combined to produce the hypothetical half-ordered **AA'** (=**BC**) structure, the hypothetical fully-ordered **BB** structure, and the disordered **CC** structure (parent melilite). The fractional population of each site is shown next to each structure. Note that **BB** contains pairs of edge-sharing *RE*2 sites (black outline), whilst **AA'** contains a low population of *RE*2 sites (1/4). The intergrowth of **AA'** and **BB** fragments to form **ABA'** eliminates *RE*2-*RE*2 edge-sharing by reducing the population of *RE*2 sites to an intermediate value (1/3).

The underlying melilite structure can be described as a hexagonal tiling ("MacMahon's net" or "Cairo pentagonal tiling" corresponding to a pair of orthogonal interpenetrating hexagonal nets),[51,52] as illustrated in Figure 10b. Here, it can be seen that two tile types **A** and **B** are required to describe the structure fully, and these tessellate in stripes along the *b* axis (Figure 10b) in sequence **ABA'** (where **A'** = 180° rotation of **A**) to produce the observed 3-fold unit cell expansion. Tile **A** is a half-ordered structural fragment containing 1x Sr site, 1x *RE* site and 2x mixed sites. Tile **B** is a fully-ordered structural fragment containing 2x Sr sites and 2x *RE* sites, corresponding to fully-ordered structural fragment. **ABA'** is therefore 2/3-ordered. For the purpose of discussion, a fully-disordered structural fragment (tile **C**) is also illustrated in Figure 10c.

The stability of **ABA'** tiling can be explained by comparison with the simpler hypothetical structures produced by its individual components **A** and **B**. It can

be seen that **AA**' (= **BC**) tiling supports a wide separation of the small highly-distorted *RE*2 sites with no requirement for edge-sharing between the highly distorted *RE*2 pentagonal channels, but it produces a low overall population of these sites (1/4), with half of the cations accommodated on mixed sites. This hypothetical half-ordered structure is disfavored, because it does not maximize the number of small *RE*2 sites available for the [6+1] coordination of RE^{3+}. In contrast, the hypothetical fully-ordered structure afforded by **BB** tiling yields the highest possible population of *RE*2 sites (1/2), but it is disfavored because it requires each of these highly-distorted channels to share edges (as indicated by the black outline in Figure 10c). It follows that the **ABA**' tiling is a compromise between the local bonding preferences of the small *RE* cation (which demands a high population of [6+1] *RE*2 sites) and the limited flexibility of the host framework which cannot distort to support two such sites in close proximity locally. The 3x1x1 superstructure thus retains 1/3 of its A-sites as mixed sites, which are larger and less distorted than *RE*2, as a buffer between the fully-ordered fragments. This maximizes the *RE*2 [6+1] population, whilst keeping the Ga_3O_7 framework strain to within acceptable limits.

4.2 Competition between ordered and disordered polymorphs. The trends in thermodynamic and structural stability in the Sr*RE*Ga_3O_7 series depend strongly on the ionic radius of the *RE* cation (Figure 8). The 3x1x1 superstructure is most stable when the cation mismatch is largest: the Lu member is ordered over its entire stability range, and the Yb member has a very strong tendency towards ordering with only a narrow window between its cation-disordering and decomposition temperatures. As the *RE* ionic radius increases, the stability of the superstructure decreases until the disordered polymorph becomes dominant when *RE* is larger than Er. This trend can also be seen in the fact that $SrErGa_3O_7$ and $SrTmGa_3O_7$ are readily synthesized in their ordered polymorphs by ex-situ crystallization in a muffle furnace, whilst in $SrDyGa_3O_7$ and $SrHoGa_3O_7$ the 3x1x1 superstructure can only be obtained by precise control of the annealing protocol (see section 3.4). $SrYGa_3O_7$ presents an intermediate case, with isolated fully-ordered nano-domains forming on ex-situ crystallization. Eventually, when the *RE* radius becomes sufficiently large (*RE* = Tb), cation ordering is no longer observed. This trend is consistent with the nature of the superstructure itself: the distortion of the Ga_3O_7 framework to generate a set of highly distorted pentagonal channels that accommodate *RE* in [6+1] coordination requires A site cations that are small enough to occupy such a site. This implies that the formation of the 3x1x1 superstructure is dependent not only upon Sr/*RE* size mismatch, but is also conditional upon the absolute size of the *RE* cation. For example, this may explain why the Ba-based melilites $BaNdGa_3O_7$ (A-site ionic radius radio r_{Ba}/r_{Nd} = 1.28, assuming 8-fold coordination) and $BaSmGa_3O_7$ (r_{Ba}/r_{Sm} = 1.32)[6] adopt the tetragonal *P*-42$_1$*m* structure despite having Ba/*RE* radius ratios that are similar to $SrYbGa_3O_7$ (r_{Sr}/r_{Yb} = 1.28), as Nd^{3+} and Sm^{3+} are too large to tolerate [6+1] coordination. The opposite case is presented by $CaErGa_3O_7$[6]: this compound is reported to adopt the tetragonal parent structure despite the presence of the small Er^{3+} cation, which may be because the relatively weak size contrast between Ca^{2+} and Er^{3+} (r_{Ca}/r_{Er} = 1.12) is insufficient to drive long range ordering. These examples suggest that both a large A-cation size contrast (e.g. $AE^{2+}/RE^{3+} \approx 1.28$), and a sufficiently small *RE* cation (Dy^{3+} or smaller), must be present together to stabilize the 3x1x1 superstructure.

Alternative framework distortions that are available to small-cation melilite gallates are the 5D modulated structures of $CaLaGa_3O_7$ and $CaNdGa_3O_7$. In these compounds, a pair of modulation vectors parallel to the basal axes of the tetragonal melilite parent cell generate a set of 6-, 7- and 8-coordinate A sites (versus 8-coordinate-only in the tetragonal parent phase). The population of these sites by Ca and *RE* is non-random, with Ca showing a preference for the 6-coordinate sites (e.g. these sites are approximately 60% occupied by Ca and 40% by Nd in $CaNdGa_3O_7$). In these compounds, the average A-site cation radius (e.g. 1.115 Å for $CaNdGa_3O_7$) is comparable to that found in $SrYbGa_3O_7$ (1.123 Å), and this drives the distortion of the framework to reduce the average size of the channels, although the 6-coordinate channels exhibited by $CaNdGa_3O_7$ (six A-O distances of 2.4 – 2.7 Å and two of 2.9 – 3.1 Å) are not as small or distorted as those found in the 3x1x1 superstructure of $SrYbGa_3O_7$ (six distances of 2.22 – 2.52 Å and one of 2.97 Å). The relatively low contrast in ionic radii between Ca/Nd (= 1.01) may not provide a sufficient driving force for full cation ordering such as that found in the 3x1x1 superstructure (Sr/Yb = 1.28). Note that the absence of satellite peaks in the SAED patterns of quenched $SrTmGa_3O_7$ (which adopts tetragonal parent structure, as described in section 3.2) (Figure S4) is consistent with the conclusions of Wei *et. al.*[8], who describe the relationship between structural modulation and *A/B* cation radius ratio: whilst it is close to the proposed boundary, the average *A* site cation radius in

$SrTmGa_3O_7$ is not sufficiently small to induce modulation.

In summary, the interplay between the tetragonal parent structure, the 5D modulated structures and the 3x1x1 superstructure is governed by the average size of the A-site cations (a small average radius is required for the modulated structures and 3x1x1 superstructures); the contrast between the A site radii (high contrast favors the 3x1x1 superstructure over the modulated structures); and the absolute ionic radius of the *RE* cation (3x1x1 superstructure is only stable if *RE* < Tb^{3+}), as shown schematically in Figure 11.

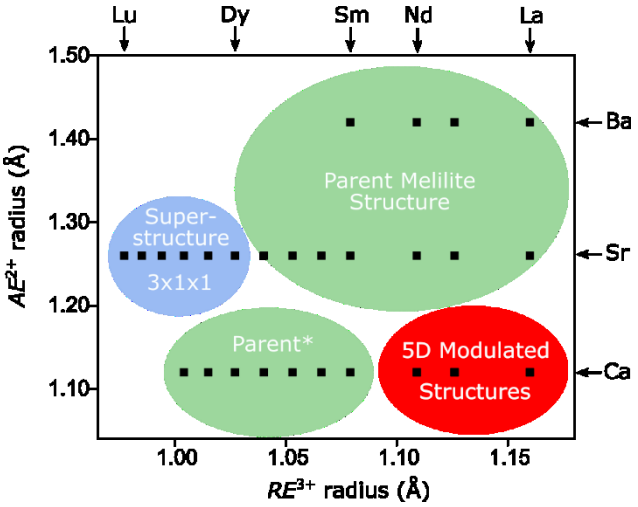

Figure 11. Phase diagram indicating the different structural orderings reported for the (*AE,RE*)Ga_3O_7 melilite family, according to the ionic radii of their A site cations. The parent structure and 5D-modulated structure regions have been compiled from the literature[6,8,12]. Note that the parent structure region for *AE* = Ca, marked with an asterisk, was reported prior to the discovery of structural modulation in $CaLaGa_3O_7$ and $CaNdGa_3O_7$.

4.3 Effect of structural ordering on optical properties. The structural ordering of the Sr*RE*Ga_3O_7 melilites leads to a decrease of their optical transmission in the bulk form (Figure S15), resulting from light scattering losses at the grain boundaries, as well-known and described in the literature[15,53]. This effect is particularly pronounced in the short wavelength region and can also affect the maximum transmission of the bulk ceramic.

The photoluminescence spectroscopic properties of *RE* doped glass-ceramics have been intensively studied in the past 20 years[54–57]. It is commonly accepted that structural ordering around the *RE* ions resulting from controlled crystallization of their parent glasses can significantly modify their emission features by increasing their emission intensities for instance. Such enhancement can be particularly strong (over 100x) when energy levels of the *RE* ions are more efficiently excited through energy transfers between the *RE* ions after their incorporation into the crystalline phase. Their migration within the material can also lead to an optimized *RE* interionic distance favorable to these energy transfers. The absorption and emission band shapes of *RE* ions in structured environment are expected to be affected, by showing a narrower linewidth and more intense absorption/emission peaks, similarly to that observed in single crystals[54–57].

Here, a clear structuration of the absorption bands of the Sr*RE*Ga_3O_7 ceramic melilites is observed (Figure S16), thus illustrating this structural ordering around the *RE* ions. Then, the increase of intensity observed in the emission spectra recorded on the $SrErGa_3O_7$ bulk ceramic (Figure S17) can be mostly attributed to the light scattering induced by grain boundaries and the experimental technique used to excite and collect emitted light. Both excitation and emission light pathways are indeed expanded in the transparent bulk ceramic in comparison with the glass. This assumption is clearly supported by the emission spectra presented in Figure 9, where the glass and ceramic melilites were finely crushed to obtain comparable grain size, minimizing therefore the scattering related to the sample textures/morphologies. The observed increase of Er^{3+} emission intensity in the ceramic *vs* the glass powdered melilites is then not as high as that observed in the bulk's measurement (Figure S17).

Nevertheless, as one can observe in Figure 9, there is a notable difference of spectral emission line shapes between the disordered and ordered ceramics. The strong structuration of the emission band observed in the ordered melilite ceramic can be compared, to some extent, to the sharp spectral bands of Er^{3+} in YAG single crystals and transparent ceramics[58], indicating a long-range ordering. The structural environment of the *RE* ions is well defined and identical across the material, resulting in these sharper band features. On the other hand, the emission line shape of the disordered ceramic is continuously broadened and very similar to that of the glass, indicating that the *RE* environment in the glass and disordered are close.

The near and mid-infrared emission bands of the Sr*RE*Ga_3O_7 melilites make them potential candidates for the development of infrared solid state lasers and compact sources for dentistry, surgery, remote sensing, environment, and security and defense,[59–64] which should motivate further spectroscopic study of these materials in the 2-5 µm range, for example using low temperature conditions and/or time resolved spectroscopy.

5. CONCLUSION

We have shown that the glass crystallization method can be used to synthesize a series of small rare-earth melilites Sr*RE*Ga_3O_7 (*RE* = Dy – Lu, Y) with control of their crystal structures and luminescence properties. These compounds are found to be metastable, with thermal decomposition temperatures in the range 800 – 850°C for the smallest rare-earths Ho - Lu, which makes them challenging to access by conventional high-temperature ceramic methods. By tuning the crystallization conditions, we have shown that it is possible to isolate two different crystal structures for each composition. The first is a conventional tetragonal melilite structure with fully disordered A site cations, which forms readily for the larger rare-earth members *RE* = Dy – Er, but can also be obtained for the smaller rare-earth members (all except *RE* = Lu) by rapid quenching from high temperature. The second accessible crystal structure is a 3x1x1 melilite superstructure with Sr and *RE* ordered over three distinct A sites of equal multiplicity (Sr-only, *RE*-only and mixed Sr/*RE*), which is strongly favored for the smallest rare-earth members *RE* = Tm, Yb and Lu, but can also be isolated for the larger members Dy – Er and Y by appropriate control of heating and cooling rates during crystallization. In this structure, cation ordering is driven by the bonding requirements of the small *RE* cation, which adopts a highly distorted [6+1] coordination. The host Ga_3O_7 framework accommodates these [6+1] sites in a pseudo-hexagonal arrangement which maximizes their separation but limits their population to 1/3 of the A sites. This competition between the bonding demands of RE^{3+} and the flexibility of the host framework favors the retention of the mixed Sr/*RE* site (population 1/3) which acts as a buffer between fully-ordered structural fragments. The 3x1x1 superstructure offers an alternative way to order small A cations in the melilite structure, which contrasts with the previously reported modulated distortions in Ca-based analogues $CaLaGa_3O_7$ and $CaNdGa_3O_7$ which are partially cation-ordered. We propose that the particular combination of average A-site size (ionic radius), A-site size contrast, and absolute size of the *RE* cation are the key parameters that control the ordering type in these structures, and note that the 3x1x1 structures and modulated structures occupy two distinct regions of this parameter space. Finally, we show that the control of cationic ordering around Er^{3+} ions in $SrErGa_3O_7$ ceramics influences the luminescence properties, revealing a comparable structural environment in both disordered ceramics and glasses, whilst samples that adopt long range ordering of Sr/Er in the 3x1x1 superstructure produces sharper spectral bands that are reminiscent of YAG single crystals or transparent ceramics. With their broad optical transmission range (extending up to 6-7 μm wavelengths) and ease of fabrication, the Sr*RE*Ga_3O_7 glass and ceramic melilites appear to be promising *RE* host materials for active photonic applications.

ASSOCIATED CONTENT

SUPPORTING INFORMATION.

Table S1. Refined anisotropic thermal parameters obtained from SPD and NPD data collected at room temperature on cation-ordered $SrYbGa_3O_7$ ($P2_12_12$ space group, a = 23.70164(7) Å, b = 7.92109(3) Å and c = 5.21162(2) Å). This materials supplements Table 1 of the main manuscript.

Table S2. Refined Ga-O interatomic distances obtained from cation-ordered $SrYbGa_3O_7$ from SPD and NPD data. This material supplements Table 2 of the main manuscript.

Table S3. Refined structural parameters obtained from SPD data collected at room temperature on cation-ordered $SrTmGa_3O_7$ ($P2_12_12$ space group, a = 23.74405(8) Å, b = 7.92635(3) Å and c = 5.21619(2) Å).

Table S4. Refined interatomic distances ($d_{A\text{-}O}$ up to 3 Å) obtained from cation-ordered $SrTmGa_3O_7$ from SPD data.

Tables S5. Refined structural parameters obtained from SPD data collected at room temperature on cation-ordered $SrErGa_3O_7$ ($P2_12_12$ space group, a = 23.7790(1) Å, b = 7.93013(4) Å and c = 5.22786(2) Å).

Table S6. Refined interatomic distances ($d_{A\text{-}O}$ up to 3 Å) obtained from cation-ordered $SrErGa_3O_7$ from SPD data.

Tables S7. Refined structural parameters obtained from SPD data collected at room temperature on cation-ordered $SrHoGa_3O_7$ from SPD data ($P2_12_12$ space group, a = 23.8034(1) Å, b = 7.93800(4) Å and c = 5.23828(2) Å).

Table S8. Refined interatomic distances ($d_{A\text{-}O}$ up to 3 Å) obtained in cation-ordered $SrHoGa_3O_7$ from SPD data.

Tables S9. Refined structural parameters obtained from SPD data collected at room temperature on cation-ordered $SrLuGa_3O_7$ ($P2_12_12$ space group, a = 23.6710(2) Å, b = 7.91556(8) Å and c = 5.20516(4) Å). Note that the oxide *x, y, z* coordinates and *U* values were subjected to soft restraints to keep them close to the corresponding values from $SrYbGa_3O_7$ (see main text).

Table S10. Interatomic distances ($d_{A\text{-}O}$ up to 3 Å) obtained in cation-ordered $SrLuGa_3O_7$ from SPD data. Note that the oxygens *x, y, z* coordinates and *U* values were subjected to soft restraints to keep them close to the corresponding values from $SrYbGa_3O_7$.

Tables S11. Refined structural parameters obtained from laboratory PXRD data collected at room temperature on cation-ordered $SrDyGa_3O_7$ from laboratory PXRD data ($P2_12_12$ space group, a = 23.8404(3) Å, b = 7.9510(1) Å and c = 5.24314(2).

Table S12. Refined interatomic distances ($d_{A\text{-}O}$ up to 3 Å) obtained from cation-ordered $SrDyGa_3O_7$ from laboratory PXRD data.

Table S13. Refined structural parameters of disordered $SrYbGa_3O_7$ from laboratory PXRD data (P-42$_1$m space group, $a = b$ = 7.91985(9) Å and c = 5.21070(7) Å).

Table S14. Refined interatomic distances of disordered $SrYbGa_3O_7$ from laboratory PXRD data.

Table S15. Refined structural parameters of disordered $SrTmGa_3O_7$ from SPD data (P-42$_1$m space group, $a = b$ = 7.92455(3) Å, and c = 5.21558(2) Å).

Table S16. Refined interatomic distances of disordered from SPD data $SrTmGa_3O_7$.
Table S17. Refined structural parameters of disordered $SrErGa_3O_7$ from SPD data (P-42_1m space group, $a = b = 7.93227(2)$ Å, and $c = 5.22367(2)$ Å).
Table S18. Refined interatomic distances of disordered $SrErGa_3O_7$ from SPD data.
Table S19. Refined structural parameters of disordered $SrHoGa_3O_7$ from laboratory PXRD data (P-42_1m space group, $a = b = 7.93999(2)$ Å, and $c = 5.23060(2)$ Å, Rp= 1.413% Rwp= 2.081%).
Table S20. Refined interatomic distances of disordered $SrHoGa_3O_7$ from laboratory PXRD data.
Figure S1. Laboratory X-ray powder diffraction data of $SrREGa_3O_7$ (RE = Tb-Lu, Y) glass samples synthesized by aerodynamic levitation coupled to laser heating (ADL).
Figure S2. In situ X-ray powder diffraction data of the nominal $SrYbGa_3O_7$ composition recorded from 500°C up to 1500 °C (no phase modification occurs between room temperature and 500°C). The different colors correspond to the indexation of $SrCO_3$ (black), Yb_2O_3 (blue), Ga_2O_3 (green), $SrGa_2O_4$ (pink) and $Yb_3Ga_5O_{12}$ (purple). From room temperature to 900°C only the $SrCO_3$, Yb_2O_3 and Ga_2O_3 precursors are present. At 900°C $SrCO_3$ reacts with Ga_2O_3 to form $SrGa_2O_4$. At 1250°C Yb_2O_3 and residual Ga_2O_3 react to form the $Yb_3Ga_5O_{12}$ garnet and the other crystalline phases melt from 1350°C.
Figure S3. (a) Photograph of the $SrREGa_3O_7$ polished glass and ceramic materials (from Boyer et al., J. Mater. Chem. C, 2016, 4, 3238). (b) Bright field TEM micrograph of the $SrYbGa_3O_7$ transparent ceramic showing a wide grain size distribution and the absence of residual glass, porosity or secondary phase.
Figure S4. [001]* Selected Area Electron Diffraction pattern of disordered $SrTmGa_3O_7$ melilite parent synthesized by rapid quenching from the high-temperature disordered domain. The indexation of the classic tetragonal melilite structure (a=7.9 Å x c = 5.2 Å, P-42_1m) is reported and the arrows point the reflections assigned to double diffraction.
Figure S5. Post-DSC PXRD data of Sr*RE*Ga_3O_7, where black and dark blue tick marks correspond to the $P2_12_12$ 3x1x1 ordered superstructure (exhibited by *RE* = Dy – Lu, Y) and the P-42_1m disordered structure (exhibited by $SrTbGa_3O_7$ only) respectively.
Figure S6. Glass, ordered and disordered melilite Sr*RE*Ga_3O_7 (*RE* =Tb – Lu, Y) domains of stability on (a) heating and (b) cooling at rates of 10°C min^{-1}, drawn from DSC results (Figure 7, main manuscript) and PXRD measurements performed post-DSC (Figure S5).
Figure S7. Rietveld refinement of a) disordered $SrYbGa_3O_7$ (laboratory PXRD data, R_p = 2.87% R_{wp} = 3.83%) and b) disordered $SrTmGa_3O_7$ (SPD data, R_p = 6.36% R_{wp} = 8.32%). Observed (black dot), calculated (red line), and difference (blue line) profiles are shown. The set of green vertical lines corresponds to reflection positions.
Figure S8. Rietveld refinement of a) disordered $SrErGa_3O_7$ (SPD data, R_p = 6.78% R_{wp} = 8.75 %) and b) $SrHoGa_3O_7$ disordered melilite (laboratory PXRD data, R_p = 1.41% R_{wp} = 2.08%). Observed (black dot), calculated (red line), and difference (blue line) profiles are shown. The set of green vertical lines corresponds to reflection positions.
Figure S9. Normalized synchrotron powder diffraction (SPD) data of Sr*RE*Ga_3O_7 (*RE* = Ho, Er, Tm, Yb and Lu) and laboratory powder diffraction data collected on $SrDyGa_3O_7$. Red marks correspond to the 3x1x1 melilite supercell (orthorhombic, $P2_12_12$, $a \approx 23.7$ Å, $b \approx 7.9$ Å and $c \approx 5.2$ Å), and blue marks to the classic melilite cell (tetragonal, P-42_1m, $a = 7.9$ Å x $c = 5.2$ Å).
Figure S10. Rietveld refinement of a) $SrTmGa_3O_7$ (R_p = 5.28% R_{wp} = 7.06%) and b) $SrErGa_3O_7$ (R_p = 6.70% R_{wp} = 8.60%) ordered melilites (SPD data). Observed (black dot), calculated (red line), and difference (blue line) profiles are shown. The set of green vertical lines corresponds to reflection positions.
Figure S11. Rietveld refinement of a) $SrHoGa_3O_7$ (R_p = 4.85% R_{wp} = 6.30%) and b) $SrLuGa_3O_7$ (R_p = 6.87% R_{wp} = 9.18%) ordered melilites (SPD data). Observed (black dot), calculated (red line), and difference (blue line) profiles are shown. The set of green vertical lines corresponds to reflection positions.
Figure S12. Rietveld refinement of $SrDyGa_3O_7$ ordered melilite (laboratory data, R_p = 1.66% R_{wp} = 2.21%). Observed (black dot), calculated (red line), and difference (blue line) profiles are shown. The set of green vertical lines corresponds to reflection positions.
Figure S13. [001]* HRTEM image and associated FFTs of the $SrYGa_3O_7$ melilite parent synthesized by full crystallization from glass. Disordered classic tetragonal P-42_1m melilite structure and ordered 3x1x1 $P2_12_12$ melilite supercell coexist like close neighboring nanodomains.
Figure S14. Evolution of the unit cell volume across the $SrREGa_3O_7$ (*RE* = Dy – Lu) series. *RE* = Dy was chosen as V_0. The cell volume for $SrLaGa_3O_7$ is added for comparison.
Figure S15. Optical transmission windows of the $SrHoGa_3O_7$ (a), $SrErGa_3O_7$ (b), $SrTmGa_3O_7$ (c), and $SrYbGa_3O_7$ (d) glass and ceramic melilites, recorded by UV-visible-NIR and FTIR transmission spectroscopies and normalized for 1 mm thickness[27].
Figure S16. Absorption coefficient spectra of the $SrHoGa_3O_7$ (a), $SrErGa_3O_7$ (b), $SrTmGa_3O_7$ (c), and $SrYbGa_3O_7$ (d) glass and ceramic melilites. Data were not corrected with respect to Fresnel optical losses; the increase of background absorption observed in the ceramics' spectra is due to scattering losses (see Figure S15).
Figure S17. Emission photoluminescence spectra recorded on polished bulk Sr*Er*Ga_3O_7 glass and ceramic melilites, under 520 nm excitation wavelength (from Xe lamp). Data were collected in the strictly same conditions.

Crystallographic information for Sr*RE*Ga_3O_7 (*RE* = Dy – Lu) superstructure melilite (CIF files): CCDC 2081671 (Tm, ordered), 2081672 (Lu, ordered), 2081673 (Ho, ordered), 2081674 (Er, ordered), 2081675 (Dy, ordered), 2081676 (Yb, ordered); and CCDC 2081688 (Er, disordered), 2081689 (Ho, disordered), 2081690 (Yb, disordered), 2081691 (Dy, disordered) and 2081692 (Tm, disordered) contain the supplementary crystallographic data for this paper.
These data can be obtained free of charge via www.ccdc.cam.ac.uk/data_request/cif, or by emailing data_request@ccdc.cam.ac.uk, or by contacting The Cambridge Crystallographic Data Centre, 12 Union Road, Cambridge CB2 1EZ, UK; fax: +44 1223 336033.

AUTHOR INFORMATION

Corresponding Author

* E-mail : mathieu.allix@cnrs-orleans.fr
* E-mail : michael.pitcher@cnrs-orleans.fr

ACKNOWLEDGMENT

Use of the Advanced Photon Source at Argonne National Laboratory was supported by the U. S. Depart-

ment of Energy, Office of Science, Office of Basic Energy Sciences, under Contract No. DE-AC02-06CH11357. The authors acknowledge Dr. F. Porcher for neutron experiments which were performed at the Laboratoire Léon Brillouin in Saclay (France). The authors thank the ICMN and CME laboratories (Orléans, France) for CM20 TEM and PIPS access respectively. This project has benefited from the facilities of the Platform MACLE-CVL. This project is co-funded by the European Union, the Région - Centre Val de Loire and the French minister of research (MESRI - DRRT). Europe is committed to the Centre-Val de Loire region with the European regional development fund (ERDF). MP acknowledges funding from the Agence Nationale de la Recherche (project CAPRE). The authors also acknowledge the Canadian Excellence Research Chair program (CERC) in Photonics Innovations, the Fonds de Recherche Québécois sur la Nature et les Technologies (FRQNT) and the Canadian Foundation for Innovation (CFI).

REFERENCES

(1) Zhang, Y.; Yin, X.; Yu, H.; Cong, H.; Zhang, H.; Wang, J.; Boughton, R. I. Growth and Piezoelectric Properties of Melilite ABC3O7 Crystals. *Cryst. Growth Des.* **2012**, *12* (2), 622–628. https://doi.org/10.1021/cg2007205.

(2) Karbowiak, M.; Gnutek, P.; Rudowicz, C.; Ryba-Romanowski, W. Crystal-Field Analysis for RE3+ Ions in Laser Materials: II. Absorption Spectra and Energy Levels Calculations for Nd3+ Ions Doped into SrLaGa3O7 and BaLaGa3O7 Crystals and Tm3+ Ions in SrGdGa3O7. *Chem. Phys.* **2011**, *387* (1), 69–78. https://doi.org/10.1016/j.chemphys.2011.06.036.

(3) Xia, H.; Feng, J.; Wang, Y.; Li, J.; Jia, Z.; Tu, C. Evaluation of Spectroscopic Properties of Er3+/Yb3+/Pr3+: SrGdGa3O7 Crystal for Use in Mid-Infrared Lasers. *Sci. Rep.* **2015**, *5* (1), 13988. https://doi.org/10.1038/srep13988.

(4) Kaminskii, A. A.; Yu, H. H.; Wang, J. Y.; Zhang, Y. Y.; Zhang, H. J.; Lux, O.; Rhee, H.; Eichler, H. J.; Hanuza, J.; Yoneda, H.; Shirakawa, A. Tetragonal SrGdGa3O7and SrLaGa3O7—Novel SRS-Active Crystals. *Laser Phys.* **2014**, *24* (8), 085803. https://doi.org/10.1088/1054-660X/24/8/085803.

(5) Zhang, X.; Zhang, J.; Liang, L.; Su, Q. Luminescence of SrGdGa3O7:RE3+(RE=Eu, Tb) Phosphors and Energy Transfer from Gd3+ to RE3+. *Mater. Res. Bull.* **2005**, *40* (2), 281–288. https://doi.org/10.1016/j.materresbull.2004.10.011.

(6) Skakle, J. M. S.; Herd, R. Crystal Chemistry of (RE, A)2M3O7 Compounds (RE=Y, Lanthanide; A=Ba, Sr, Ca; M=Al, Ga). *Powder Diffr.* **1999**, *14* (3), 195–202. https://doi.org/10.1017/S0885715600010526.

(7) Boyer, M.; Carrion, A. J. F.; Ory, S.; Becerro, A. I.; Villette, S.; Eliseeva, S. V.; Petoud, S.; Aballea, P.; Matzen, G.; Allix, M. Transparent Polycrystalline $SrREGa_3O_7$ Melilite Ceramics: Potential Phosphors for Tuneable Solid State Lighting. *J. Mater. Chem. C* **2016**, *4* (15), 3238–3247. https://doi.org/10.1039/C6TC00633G.

(8) Wei, F.; Baikie, T.; An, T.; Kloc, C.; Wei, J.; White, T. Crystal Chemistry of Melilite [CaLa]2[Ga]2[Ga2O7]2: A Five Dimensional Solid Electrolyte. *Inorg. Chem.* **2012**, *51* (10), 5941–5949. https://doi.org/10.1021/ic300585t.

(9) Seifert, F.; Czank, M.; Simons, B.; Schmahl, W. A Commensurate-Incommensurate Phase Transition in Iron-Bearing Åkermanites. *Phys. Chem. Miner.* **1987**, *14* (1), 26–35. https://doi.org/10.1007/BF00311145.

(10) Hemingway, B. S.; Evans, H. T.; Nord, G. L.; Haselton, H. T. Akermanite: Phase Transitions in Heat Capacity and Thermal Expansion and Revised Thermodynamic Data. 10.

(11) Hagiya, K.; Ohmasa, M.; Iishi, K. The Modulated Structure of Synthetic Co-Åkermanite, Ca2CoSi2O7. *Acta Crystallogr. B* **1993**, *49* (2), 172–179. https://doi.org/10.1107/S0108768192008048.

(12) Wei, F.; Baikie, T.; An, T.; Schreyer, M.; Kloc, C.; White, T. J. Five-Dimensional Incommensurate Structure of the Melilite Electrolyte [CaNd]2[Ga]2[Ga2O7]2. *J. Am. Chem. Soc.* **2011**, *133* (38), 15200–15211. https://doi.org/10.1021/ja206441x.

(13) Xiao, Z.; Yu, S.; Li, Y.; Ruan, S.; Kong, L. B.; Huang, Q.; Huang, Z.; Zhou, K.; Su, H.; Yao, Z.; Que, W.; Liu, Y.; Zhang, T.; Wang, J.; Liu, P.; Shen, D.; Allix, M.; Zhang, J.; Tang, D. Materials Development and Potential Applications of Transparent Ceramics: A Review. *Mater. Sci. Eng. R Rep.* **2020**, *139*, 100518. https://doi.org/10.1016/j.mser.2019.100518.

(14) Won, R. Ceramic Future. *Nat. Photonics* **2008**, *2* (4), 216–217. https://doi.org/10.1038/nphoton.2008.46.

(15) Ikesue, A.; Aung, Y. L. Ceramic Laser Materials. *Nat. Photonics* **2008**, *2* (12), 721–727. https://doi.org/10.1038/nphoton.2008.243.

(16) Krell, A.; Klimke, J.; Hutzler, T. Transparent Compact Ceramics: Inherent Physical Issues. *Opt. Mater.* **2009**, *31* (8), 1144–1150. https://doi.org/10.1016/j.optmat.2008.12.009.

(17) Chen, S.; Wu, Y. New Opportunities for Transparent Ceramics. *Am. Ceram. Soc. Bull.* **2013**, *92* (2), 32–37.

(18) Goldstein, A.; Krell, A. Transparent Ceramics at 50: Progress Made and Further Prospects. *J. Am. Ceram. Soc.* **2016**, *99* (10), 3173–3197. https://doi.org/10.1111/jace.14553.

(19) Apetz, R.; Bruggen, M. P. B. van. Transparent Alumina: A Light-Scattering Model. *J. Am. Ceram. Soc.* **2003**, *86* (3), 480–486. https://doi.org/10.1111/j.1151-2916.2003.tb03325.x.

(20) Messing, G. L.; Stevenson, A. J. Toward Pore-Free Ceramics. *Science* **2008**, *322* (5900), 383–384. https://doi.org/10.1126/science.1160903.

(21) Allix, M.; Alahrache, S.; Fayon, F.; Suchomel, M.; Porcher, F.; Cardinal, T.; Matzen, G. Highly Transparent $BaAl_4O7$ Polycrystalline Ceramic Obtained by Full Crystallization from Glass. *Adv. Mater.* **2012**, *24* (41), 5570–5575. https://doi.org/10.1002/adma.201202282.

(22) Al Saghir, K.; Chenu, S.; Veron, E.; Fayon, F.; Suchomel, M.; Genevois, C.; Porcher, F.; Matzen, G.; Massiot, D.; Allix, M. Transparency through Structural Disorder: A New Concept for Innovative Transparent Ceramics. *Chem. Mater.* **2015**, *27* (2), 508–514. https://doi.org/10.1021/cm5037106.

(23) Bertrand, A.; Carreaud, J.; Chenu, S.; Allix, M.; Véron, E.; Duclère, J.-R.; Launay, Y.; Hayakawa, T.; Genevois, C.; Brisset, F.; Célarié, F.; Thomas, P.; Delaizir, G. Scalable and Formable Tellurite-Based Transparent Ceramics for Near Infrared Applications. *Adv. Opt. Mater.* **2016**, *4* (10), 1482–1486. https://doi.org/10.1002/adom.201600230.

(24) Irifune, T.; Kawakami, K.; Arimoto, T.; Ohfuji, H.; Kunimoto, T.; Shinmei, T. Pressure-Induced Nano-Crystallization of Silicate Garnets from Glass. *Nat. Commun.* **2016**, *7* (1), 13753. https://doi.org/10.1038/ncomms13753.

(25) Ma, X.; Li, X.; Li, J.; Genevois, C.; Ma, B.; Etienne, A.; Wan, C.; Véron, E.; Peng, Z.; Allix, M. Pressureless Glass Crystallization of Transparent Yttrium Aluminum Garnet-Based Nanoceramics. *Nat. Commun.* **2018**, *9* (1), 1–9. https://doi.org/10.1038/s41467-018-03467-7.

(26) Boyer, M.; Yang, X.; Carrión, A. J. F.; Wang, Q.; Véron, E.; Genevois, C.; Hennet, L.; Matzen, G.; Suard, E.; Thiaudière, D.; Castro, C.; Pelloquin, D.; Kong, L. B.; Kuang, X.; Allix, M. First Transparent Oxide Ion Conducting Ceramics Synthesized by Full Crystallization from Glass. *J. Mater. Chem. A* **2018**, *6* (13), 5276–5289. https://doi.org/10.1039/C7TA07621E.

(27) Alahraché, S.; Al Saghir, K.; Chenu, S.; Véron, E.; De Sousa Meneses, D.; Becerro, A. I.; Ocaña, M.; Moretti, F.; Patton, G.;

Dujardin, C.; Cussó, F.; Guin, J.-P.; Nivard, M.; Sangleboeuf, J.-C.; Matzen, G.; Allix, M. Perfectly Transparent $Sr_3Al_2O_6$ Polycrystalline Ceramic Elaborated from Glass Crystallization. *Chem. Mater.* **2013**, *25* (20), 4017–4024. https://doi.org/10.1021/cm401953d.

(28) Wisniewski, W.; Fernández-Carrión, A. J.; Schöppe, P.; Rüssel, C.; Allix, M. Oriented Nucleation and Crystal Growth in SrO–Al_2O_3–SiO_2 Tectosilicate Glasses. *CrystEngComm* **2018**, *20* (25), 3455–3466. https://doi.org/10.1039/C8CE00231B.

(29) Boyer, M.; Alahraché, S.; Genevois, C.; Licheron, M.; Lefevre, F.-X.; Castro, C.; Bonnefont, G.; Patton, G.; Moretti, F.; Dujardin, C.; Matzen, G.; Allix, M. Enhanced Transparency through Second Phase Crystallization in BaAl4O7 Scintillating Ceramics. *Cryst. Growth Des.* **2016**, *16* (1), 386–395. https://doi.org/10.1021/acs.cgd.5b01374.

(30) Alahraché, S.; Allix, M.; Matzen, G.; Millot, F.; Licheron, M.; Cardinal, T.; Garcia, A.; Saghir, K. A. Verres, Vitroceramiques et Ceramiques d'aluminates Transparents. WO2013079707A1, **2013**.

(31) Fernandez-Carrion, A. J.; Al Saghir, K.; Veron, E.; Becerro, A. I.; Porcher, F.; Wisniewski, W.; Matzen, G.; Fayon, F.; Allix, M. Local Disorder and Tunable Luminescence in Sr1–x/2Al2–XSixO4 ($0.2 \leq x \leq 0.5$) Transparent Ceramics. *Inorg. Chem.* **2017**, *56* (23), 14446–14458. https://doi.org/10.1021/acs.inorgchem.7b01881.

(32) Rousse, G.; Baptiste, B.; Lelong, G. Crystal Structures of $Li_6B_4O_9$ and $Li_3B_{11}O_{18}$ and Application of the Dimensional Reduction Formalism to Lithium Borates. *Inorg. Chem.* **2014**, *53* (12), 6034–6041. https://doi.org/10.1021/ic500331u.

(33) Weber, J. K. R. The Containerless Synthesis of Glass. *Int. J. Appl. Glass Sci.* **2010**, *1* (3), 248–256. https://doi.org/10.1111/j.2041-1294.2010.00026.x.

(34) Coelho, A. A. TOPAS and TOPAS-Academic: An Optimization Program Integrating Computer Algebra and Crystallographic Objects Written in C++. *J. Appl. Crystallogr.* **2018**, *51* (1), 210–218. https://doi.org/10.1107/S1600576718000183.

(35) Rosenflanz, A.; Frey, M.; Endres, B.; Anderson, T.; Richards, E.; Schardt, C. Bulk Glasses and Ultrahard Nanoceramics Based on Alumina and Rare-Earth Oxides. *Nature* **2004**, *430* (7001), 761–764. https://doi.org/10.1038/nature02729.

(36) Boultif, A.; Louër, D. Indexing of Powder Diffraction Patterns for Low-Symmetry Lattices by the Successive Dichotomy Method. *J. Appl. Crystallogr.* **1991**, *24* (6), 987–993. https://doi.org/10.1107/S0021889891006441.

(37) Oszlányi, G.; Sütő, A. Ab Initio Structure Solution by Charge Flipping. *Acta Crystallogr. A* **2004**, *60* (2), 134–141. https://doi.org/10.1107/S0108767303027569.

(38) Oszlányi, G.; Sütő, A. Ab Initio Structure Solution by Charge Flipping. II. Use of Weak Reflections. *Acta Crystallogr. A* **2005**, *61* (1), 147–152. https://doi.org/10.1107/S0108767304027746.

(39) Petříček, V.; Dušek, M.; Palatinus, L. Crystallographic Computing System JANA2006: General Features. *Z. Für Krist. - Cryst. Mater.* **2014**, *229* (5), 345–352. https://doi.org/10.1515/zkri-2014-1737.

(40) Palatinus, L.; Chapuis, G. SUPERFLIP – a Computer Program for the Solution of Crystal Structures by Charge Flipping in Arbitrary Dimensions. *J. Appl. Crystallogr.* **2007**, *40* (4), 786–790. https://doi.org/10.1107/S0021889807029238.

(41) Baerlocher, C.; McCusker, L. B.; Palatinus, L. Charge Flipping Combined with Histogram Matching to Solve Complex Crystal Structures from Powder Diffraction Data. *Z Krist.* **2007**, *222*, 47–53.

(42) Steins, M.; Schmitz, W.; Uecker, R.; Doerschel, J. Crystal Structure of Strontium Lanthanum Trigallium Heptoxide, (Sr0.5La0.5)2Ga3O7. *Z. Für Krist. - New Cryst. Struct.* **1997**, *212* (1), 76–76. https://doi.org/10.1524/ncrs.1997.212.1.76.

(43) Pennycook, S. J.; Boatner, L. A. Chemically Sensitive Structure-Imaging with a Scanning Transmission Electron Microscope. *Nature* **1988**, *336* (6199), 565–567. https://doi.org/10.1038/336565a0.

(44) Hartel, P.; Rose, H.; Dinges, C. Conditions and Reasons for Incoherent Imaging in STEM. *Ultramicroscopy* **1996**, *63* (2), 93–114. https://doi.org/10.1016/0304-3991(96)00020-4.

(45) Pennycook, S. J.; Jesson, D. E. High-Resolution Z-Contrast Imaging of Crystals. *Ultramicroscopy* **1991**, *37* (1), 14–38. https://doi.org/10.1016/0304-3991(91)90004-P.

(46) Stadelmann, P. JEMS https://www.jems-swiss.ch/ (accessed May 4, **2020**).

(47) Van Aert, S.; Verbeeck, J.; Erni, R.; Bals, S.; Luysberg, M.; Dyck, D. V.; Tendeloo, G. V. Quantitative Atomic Resolution Mapping Using High-Angle Annular Dark Field Scanning Transmission Electron Microscopy. *Ultramicroscopy* **2009**, *109* (10), 1236–1244. https://doi.org/10.1016/j.ultramic.2009.05.010.

(48) Martinez, G. T.; Rosenauer, A.; De Backer, A.; Verbeeck, J.; Van Aert, S. Quantitative Composition Determination at the Atomic Level Using Model-Based High-Angle Annular Dark Field Scanning Transmission Electron Microscopy. *Ultramicroscopy* **2014**, *137*, 12–19. https://doi.org/10.1016/j.ultramic.2013.11.001.

(49) De Sousa Meneses, D. Focus - Curve fitting software https://www.cemhti.cnrs-orleans.fr/pot/software/focus.html (accessed Apr 7, **2020**).

(50) Scott, M.A.; Russell, D.L.; Henderson, B.; Han, T.P.J.; Gallagher, H.G. Crystal growth and optical characterisation of novel $3d^2$ ion laser hosts. *Journal of Crystal Growth* **1998**, 183 (3) 366-376. https://doi.org/10.1016/S0022-0248(97)00431-4.

(51) O'Keefe, M.; Hyde, B. G.; Anderson, J. S. Plane Nets in Crystal Chemistry. *Philos. Trans. R. Soc. Lond. Ser. Math. Phys. Sci.* **1980**, *295* (1417), 553–618. https://doi.org/10.1098/rsta.1980.0150.

(52) Fan, J.; Sarou-Kanian, V.; Yang, X.; Diaz-Lopez, M.; Fayon, F.; Kuang, X.; Pitcher, M. J.; Allix, M. $La_2Ga_3O_{7.5}$: A Metastable Ternary Melilite with a Super-Excess of Interstitial Oxide Ions Synthesized by Direct Crystallization of the Melt. *Chem. Mater.* **2020**, *32* (20), 9016–9025. https://doi.org/10.1021/acs.chemmater.0c03441.

(53) Hendy, S. Light Scattering in Transparent Glass Ceramics. *Appl. Phys. Lett.* **2002**, *81* (7), 1171–1173. https://doi.org/10.1063/1.1499989.

(54) Fedorov, P. P.; Luginina, A. A.; Popov, A. I. Transparent Oxyfluoride Glass Ceramics. *J. Fluor. Chem.* **2015**, *172*, 22–50. https://doi.org/10.1016/j.jfluchem.2015.01.009.

(55) Neuville, D. R.; Cornier, L.; Caurant, D.; Montagne, L. *From Glass to Crystal*; EDP Sciences, **2021**.

(56) Liu, X.; Zhou, J.; Zhou, S.; Yue, Y.; Qiu, J. Transparent Glass-Ceramics Functionalized by Dispersed Crystals. *Prog. Mater. Sci.* **2018**, *97*, 38–96. https://doi.org/10.1016/j.pmatsci.2018.02.006.

(57) Pablos-Martín, A. de; Durán, A.; Pascual, M. J. Nanocrystallisation in Oxyfluoride Systems: Mechanisms of Crystallisation and Photonic Properties. *Int. Mater. Rev.* **2012**, *57* (3), 165–186. https://doi.org/10.1179/1743280411Y.0000000004.

(58) Yang, H.; Zhang, J.; Luo, D.; Lin, H.; Shen, D.; Tang, D. Novel Transparent Ceramics for Solid-State Lasers. *High Power Laser Sci. Eng.* **2013**, *1* (3–4), 138–147. https://doi.org/10.1017/hpl.2013.18.

(59) Verma, S. K.; Maheshwari, S.; Singh, R. K.; Chaudhari, P. K. Laser in Dentistry: An Innovative Tool in Modern Dental Practice. *Natl. J. Maxillofac. Surg.* **2012**, *3* (2), 124–132. https://doi.org/10.4103/0975-5950.111342.

(60) Jean, B.; Bende, T. Mid-IR Laser Applications in Medicine. In *Solid-State Mid-Infrared Laser Sources*; Sorokina, I. T., Vodopyanov, K. L., Eds.; Topics in Applied Physics; Springer: Berlin, Heidelberg, **2003**; pp 530–565. https://doi.org/10.1007/3-540-36491-9_12.

(61) Adams, A. R.; Elliott, C. T.; Krier, A.; Murdin, B. N.; Waynant, R. W.; Ilev, I. K.; Gannot, I. Mid–Infrared Laser Applications in Medicine and Biology. *Philos. Trans. R. Soc. Lond. Ser. Math. Phys. Eng. Sci.* **2001**, *359* (1780), 635–644. https://doi.org/10.1098/rsta.2000.0747.

(62) Walsh, B. M.; Lee, H. R.; Barnes, N. P. Mid Infrared Lasers for Remote Sensing Applications. *J. Lumin.* **2016**, *169*, 400–405. https://doi.org/10.1016/j.jlumin.2015.03.004.

(63) Werle, P.; Slemr, F.; Maurer, K.; Kormann, R.; Mücke, R.; Jänker, B. Near- and Mid-Infrared Laser-Optical Sensors for Gas Analysis. *Opt. Lasers Eng.* **2002**, *37* (2), 101–114. https://doi.org/10.1016/S0143-8166(01)00092-6.

(63) Affan Ahmed, S.; Mohsin, M.; Zubair Ali, S. M. Survey and Technological Analysis of Laser and Its Defense Applications. *Def. Technol.* **2021**, *17* (2), 583–592. https://doi.org/10.1016/j.dt.2020.02.012.

Table of Contents

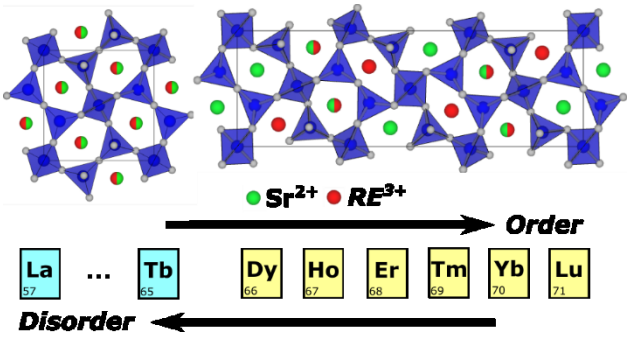

Synopsis :

A series of small-rare-earth melilites, of interest as transparent luminescent ceramics, are synthesized by glass-crystallization and show a new type of cation ordering. Their structures and stabilities are probed over multiple temperatures and length scales by high resolution diffraction and electron microscopy methods, and correlated with their photoluminescence emission spectra, demonstrating that enhanced optical properties can be obtained by minimising crystallographic disorder in the melilite structure.